MECHANISMS OF
GRAPHITE NOZZLE EROSION IN HYBRID ROCKETS

A Dissertation
Presented to
The Academic Faculty

by

[Landon T. Kamps]

In Partial Fulfillment
of the Requirements for the Degree of
Doctor of Philosophy in the
Graduate School of Engineering

Hokkaido University
September 2019

MECHANISMS OF
GRAPHITE NOZZLE EROSION IN HYBRID ROCKETS

Approved by:

Dr. Harunori Nagata, Advisor
School of Engineering
Hokkaido University

Dr. Nobuyuki Oshima
School of Engineering
Hokkaido University

Dr. Osamu Fujita
School of Engineering
Hokkaido University

Dr. Nozomu Hashimoto
School of Engineering
Hokkaido University

Date Approved:

[To the students of Hokkaido University]

ACKNOWLEDGEMENTS

This research would not have been possible without the financial and technical support of numerous organizations. These include the Japanese Ministry of Education, Science, Sports, Culture, Grant-in-Aid for Science Research (B) 15H04197 (2016), Grant-in-Aid for the Promotion of Science (JSPS) fellows 18j2087708, the matching fund program of Centers for Inter-University Collaboration from the Institute of Space and Astronautical Science (ISAS/JAXA), a collaborative research partnership with IHI Corporation, and most importantly the generous support and dedication of Tsutomu Uematsu, president of Uematsu Electric Company and co-founder of CAMUI Space Works. Tests conducted at Uematsu Electric Company were expertly managed by Mr. Hikaru Isochi, with technical support from Naoto Adachi and students of Hokkaido University. Large scale tests were designed and planned by Tor Viscor and Mitsunori Itoh of IHI Corporation, as well as Hokkaido University students Ryosuke Kawabata, Shota Hirai and Ryo Yamaguchi. Shota Hirai designed the HK/SLY-series motor, and inspired the design of the DNT-series motor. Yurika Kiyotani, Kazuhito Sakurai and Erika Uchiyama laid the groundwork for the use of nitrous oxide as an oxidizer, and Kazuhito Sakurai designed led the CBX-series campaign. Yuji Saito was paramount to the development of the comprehensive data reduction method, and a great mentor throughout this research. I owe the success of this research to the immense knowledge and pioneering attitude of Professor Harunori who guided me as my supervisor, and inspired me as a mentor. Lastly, to my wife Sayuri, who supported me with patience and love, thank you.

TABLE OF CONTENTS

LIST OF TABLES

LIST OF FIGURES

LIST OF SYMBOLS AND ABBREVIATIONS

A,b,E	=	Arrhenius equation constants
a,b,c,d	=	placeholders
CEA	=	functions representative of NASA CEA operations
c_p	=	constant pressure specific heat, J/kg-K
c^*	=	characteristic exhaust velocity, m/s
D	=	diameter, m or diffusion coefficient, m^2/s
F	=	thrust, N
k	=	thermal conductivity, W/m-K or heterogenous rate constant
M	=	mass remaining, kg
$\dot{m}$	=	mass flow/consumption rate, kg/s
P	=	pressure, Pa
Pr	=	Prandtl number
q	=	heat flux, W/m^2
R	=	radius, m or gas constant J/kg-K
R_u	=	universal gas constant, J/kmol-K
r	=	radial position from nozzle centerline, m
Δr	=	radial node spacing in the nozzle mesh, m
$\dot{r}$	=	(nozzle) erosion rate, m/s
Re	=	Reynolds number
Sc	=	Schmidt number
T	=	Temperature, K
t	=	(firing) time, s
Δt	=	time step, s
U	=	uncertainty
x,y	=	arbitrary input, output
α	=	thermal diffusivity, m^2/s
$\beta_1, \beta_2, \beta_3$	=	empirical constants in Eq. (2-17)
γ	=	specific heat ratio

ζ	=	convective heat transfer coefficient factor
η^*	=	characteristic exhaust velocity efficiency
θ	=	wall temperature factor
λ	=	thrust correction factor
μ	=	kinematic viscosity, Pa-s
ξ	=	oxidizer-to-fuel-mass ratio
ρ	=	density, kg/m^3
Φ	=	equivalence ratio
ϕ	=	partial pressure factor
Ψ,ψ	=	calculation residual terms
$\bar{}$	=	overbar, to indicate a time-averaged value

Subscripts

a	=	atmospheric
b	=	(burn) time
c	=	chamber position
calc,meas	=	distinguishes a calculated value or a measured value
e	=	nozzle exit plane position
f	=	final
fu	=	fuel
g	=	combustion gas (i.e. bulk oxidizing species)
i	=	oxidizing species index in Eq. (1) or radial node index in Eq. (29)
j	=	reaction index in Eq. (2) or time index in Eq. (29)
n	=	nozzle
n1,n2,n3	=	thermocouple positions within the nozzle
o	=	initial
on	=	onset (of nozzle erosion)
ox	=	oxidizer
t	=	nozzle throat plane position
w	=	nozzle throat wall position

Acronyms

CAMUI	=	Cascaded Multistage Impinging-jet

CEA	=	(NASA) Chemical Equilibrium with Applications
GFRP	=	Glass Fiber-Reinforced Plastic
GTO	=	Geostationary Transfer Orbit
HDPE	=	High-Density-Polyethylene
ISAS	=	Institute of Space and Astronautical Science (JAPAN)
JAXA	=	Japan Aerospace Exploration Agency
NASA	=	National Aeronautics and Space Administration (USA)
NIST	=	National Institute of Standards and Technology (USA)
NTRT	=	Nozzle Throat Reconstruction Technique
PMMA	=	Polymethyl Methacrylate
TTRT	=	Throat Temperature Reconstruction Technique

SUMMARY

This study elucidates the mechanisms of thermochemical erosion in hybrid rocket nozzles for the first time by analyzing data from over 80 hybrid rocket firing tests at various scales and thrust classes ranging from motors that are 50 mm to 300 mm in diameter at thrusts from 10 N to 2,000 N, respectively. This was only possible through the development and validation of a new data reduction methodology that enabled the determination of time-resolved nozzle throat erosion, oxidizer-to-fuel-mass ratio and nozzle throat wall temperature from measurements of thrust, chamber pressure, oxidizer mass flow rate, overall fuel mass consumption, final nozzle throat diameter, and two thermocouple measurements from within the nozzle body. Empirical analysis led to the formulation of a predictive model for nozzle erosion rate based on heterogeneous combustion theory and turbulent mass transport theory. This work is introduced in the following six chapters: (1) Nozzle Erosion in Chemical Rockets; (2) Model of Chemical Erosion; (3) Comprehensive Data Reduction; (4) Hybrid Rocket Hybrid Rocket Motor Operation; (5) Static Firing Test Results; (6) Impact on Hybrid Rocket Development.

CHAPTER 1. NOZZLE EROSION IN CHEMICAL ROCKETS

Nozzle erosion is the deterioration and regression of the surface of a nozzle due to oxidizing (chemical) reactions with, and/or physical abrasion by liquid or solid particles contained within the combustion gas flowing over it. The use of the term "erosion" may be misleading because in other context erosion is a gradual, often mechanical, removal of solid material from an object within a fluid flow. The polishing of a stone in a river bed or the deepening of a canyon by the flow of a river come to mind as more commonplace examples of erosion. In chemical rockets, the erosion of the nozzle surface is rapid, intense, and, depending on the internal ballistic conditions of the rocket, more so the result of chemical reactions than physical abrasion by the combustion gas flow. Nonetheless, the term "erosion" has been widely used as a generalization of the nozzle surface regression phenomena observed during the operation of a chemical rocket. When erosion is primarily the result of chemical reactions it is referred to as "chemical" erosion or "thermochemical" erosion. When erosion is primarily the result of physical abrasion of liquid or solid phase particles in the combustion gas, it is referred to as "mechanical" erosion.

1.1 Thermal Management of Chemical Rocket Nozzles

Chemical rocket nozzles are converging-diverging ducts that are shaped to convert the internal energy of high-pressure combustion gas to kinetic energy. A simplified depiction of a combustion chamber and nozzle is shown in Figure 1. Gas accelerates from a low velocity in the chamber, to the speed of sound at the nozzle throat, the bridge between converging and diverging sections, and beyond the speed of sound in the diverging section. Bartz demonstrated experimentally in the late 1950s and early 1960s that the convective

heat transfer coefficient, h_c W/m^2-K, in a chemical rocket nozzle is maximum at the nozzle throat where it generally reaches values on the order of ~10^4 W/m^2-K [1][2]. The adiabatic flame temperature of common chemical rocket propellant combinations is upwards of 3500 K, and the temperature decrease between the combustion chamber and the nozzle throat is usually less than 20% (i.e. less than 600 K), such that heat flux, $\dot{q}$ W/m^2, can reach values on the order of ~10^7 W/m^2.

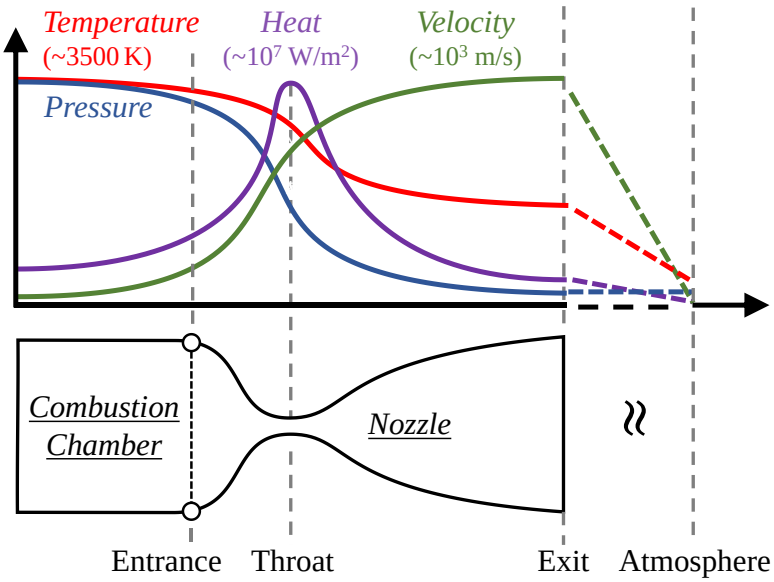

Figure 1. Conversion of internal energy to kinetic energy in a rocket nozzle.

Sutton and Biblarz summarize the most common approaches to dealing with the high heat transfer rates observed in chemical rocket combustion chambers in two categories: "steady-state" and "transient" heat transfer methods, and consider film-cooling as an "auxiliary" method [3](pp. 289). Steady-state cooling methods include convective cooling using a coolant and radiation cooling to the surroundings. Transient heat transfer methods include heat storage in the chamber material itself, and the use of ablative materials that

are consumed away during operation. The scale, operating time, payload restrictions, and the internal ballistic conditions of the rocket affect what defines the best thermal management method. However, at the nozzle throat, where heat transfer rate is largest, regenerative cooling is the most feasible steady-state method and ablative cooling is the most feasible transient method.

The use of an ablative material in the nozzle is synonymous with nozzle erosion. Nozzle erosion is used in a negative context, referring to the degradation of the nozzle resulting in a loss of rocket performance. Ablative cooling is used when nozzle erosion is accepted as a necessary loss for the preservation of the combustion chamber. Thus, the premise underlying this study is that nozzle erosion is the unavoidable consequence of rocket designs that use ablative cooling to manage thermal loads at the nozzle. Note that when an ablative is used upstream of the nozzle to invade the boundary layer at the nozzle entrance with cooler, less erosive product gas, this is considered "film cooling," not nozzle erosion. As suggested by Sutton and Biblarz in [3], film cooling is an auxiliary method that is easily implemented in conjunction with regenerative cooling and ablative cooling.

1.1.1 Regenerative Cooling of Liquid Rocket Nozzles

Liquid rockets have the option of using regenerative cooling because one of the propellants, usually the fuel, can be passed through cooling channels that encase the nozzle throat prior to being supplied to the combustion chamber. According to a recent report by Kato et al., regenerative cooling is still the most common thermal management technique in leading commercial liquid rocket engines, including the largely successful Raptor engine of SpaceX [3]. Two exceptions are the LE-8 and 30N-class liquid rockets currently being

developed by IHI Aerospace Co., Ltd. (IA), which employ ablative cooling even though regenerative cooling is a technically feasible alternative. Seeing that IA has been Japan's primary solid rocket manufacturer, the reason for the use of ablative cooling even though regenerative cooling was a reasonable alternative may be matters of (technological) heritage and cost-reduction through technology transfer within the company.

Most operational liquid rockets are regeneratively cooled by the fuel, rather than the oxidizer. The two reasons the fuel is used as the coolant over the oxidizer is that most fuels have a higher heat capacity than the oxidizers they are paired with, and fuels have very little risk of chemical interaction with the components of the feed system. In short, there is no added benefit to using the oxidizer over the fuel, whereas there is an added risk of corrosion and/or explosion within the feed system. The particulars of this tradeoff come into focus in previous research by Price [4]. Price conducted experimental investigations of regenerative cooling using liquid oxygen (LOX) as the coolant in LOX/RP-1 rocket engines with the aim of improving regenerative cooling. The motivation for running trials with LOX was that when RP-1 was used as the coolant, carbon "coke" formed along the surface of the cooling channels reducing the heat transfer efficiency and increasing the risk of thermal failure at the throat. It is not clear if similar issues have been observed in other cases. In his report, Price identified some potential hazards related to the reaction of LOX with fuel (soot) films attached to the wall near cracks in a regeneratively cooled combustion chamber. However, follow-on research by Price and Masters [5], and later by Armstrong [6], concluded that LOX could safely be used as the coolant for regenerative cooling in a liquid rocket using hydrocarbon fuels.

1.1.2 Mechanical Failure in Erosion-Resistant Nozzles

Regenerative cooling is not an option for solid rockets because the propellants are stored within the combustion chamber in the solid phase. Whereas high-conductivity copper serves as a universally adopted throat liner for regeneratively cooled nozzles, there is no material parallel in the case where no regenerative cooling is used. If there was a light-weight, anti-erosion, material capable of handling the thermal stress at the throat, solid rockets may not need to be "cooled" at all. Unfortunately, no such material has been discovered yet. In early deliberations, ceramics and refractory metals showed promise for their resistance to erosion. Olcott and Bachelor revealed that dense tungsten alloys are highly resistant to chemical erosion and demonstrate satisfactory resistance to thermal stress [7]. However, concurrent work by Johnston et al. lasting several years, in which an extensive inventory of refractory metals, refractory metal-carbines, graphites, ceramics, cermets, and fiber-reinforced plastics were tested as nozzle throat inserts in three distinct sub-scale solid rocket motors, revealed that no one material was best suited for all conditions [8]. The refractory metals and refractory compounds (i.e. metal-carbides, cermets and ceramics) were resistant to chemical erosion, but either melted or failed mechanically due to abrasion and thermal stress fractures, whereas the graphites and plastics were susceptible to chemical erosion. It is important to state that thermal-stress cracking occurred in all refractory compounds, but the nozzles remained in place and intact during operation.

Klopp summarized the major categories of materials available for use at the nozzle throat when regenerative cooling is not used in [9]. Figure 2 depicts these trade-offs, primarily in terms of the required operating pressure and size of the rocket under

consideration. Carbon-based compounds are suitable for use at the throat because they can bear the pressure, thermal gradients and temperatures under most circumstances. In special cases, such as in tactical missiles etc., very high pressures must be endured for a short duration, in which case refractory metals are more adept to handle the mechanical and thermal loads at the throat. At scales so large that nozzle erosion leads to negligible changes to nozzle throat area, erosion-prone materials such as fiber-reinforced plastics are the most economically feasible.

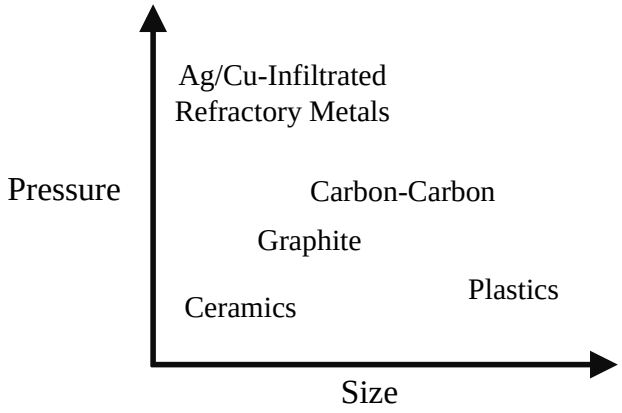

Figure 2. Material selection for the nozzle throat based on pressure and size.

1.1.3 Nozzle Erosion as Ablative Cooling in Solid Rocket Nozzles

Currently, the materials most commonly used at the nozzle throat in solid rockets are carbon-based, i.e. graphite, carbon-carbon, carbon phenolic etc. The main drawback of such materials is that they are prone to chemical erosion/oxidation [10](pp. 209). This is why, as Sutton and Biblarz state [3](pp. 567), “Almost all solid rocket nozzles are ablatively cooled.” In retrospect, the decision to move forward with ablatively cooled

nozzles was a necessary compromise given that no reasonable alternative anti-erosion material was on the shelf.

Shortly after carbon-based compounds were adopted as the primary material of choice for the nozzle throat, Parks and Bailey proposed of a way to reduce solid rocket development and operation costs through the refurbishment of ablative nozzles for reuse between firings [11]. A decade later, as part of the Alternate Nozzle Ablative Materials Program at NASA Marshall Space Flight Center and the Jet Propulsion Laboratory [12], Powers and Bailey reported the results of five firing tests that included 20 alternative carbon phenolic materials for various sections of the nozzle under consideration for use in the space shuttle solid rocket booster [13]. They concluded that Fiberite K411 Staple PAN, a graphite form carbon phenolic, is best for the nozzle throat, which in their studied had an erosion rate of only 0.05 mm/s at a chamber pressure of 6 MPa. The erosion rate of the other nine materials tested at the throat ranged from 0.09 mm/s to 0.4 mm/s.

1.1.4 Considerations for the Thermal Management of Hybrid Rocket Nozzles

In the 20th century, hybrid rockets were the subject of numerous research and development projects [14], however the focus of the chemical rocket industry as a whole was mostly split between liquid rockets and solid rockets. As a result, hybrid rocket projects were often limited to small-scale testing, with a focus on the fundamental phenomena of hybrid rocket combustion. Nozzle erosion and other topics related to the thermal management of hybrid rocket nozzles are known to be topics of importance to the success of hybrid rockets, as listed by the late Professor Kenneth Kuo in his discussion of

"Major Challenges in Hybrid Rocket Propulsion" in [15], but little work has been dedicated to addressing these issues.

In a hybrid rocket, one of the propellants is supplied to the combustion chamber as a gas or liquid droplet stream and the other propellant is stored in the combustion chamber as a solid. All major commercial hybrid rockets currently under development supply the oxidizer as the liquid and the fuel as the solid. Thus, regenerative cooling in the traditional sense, using a liquid fuel as the coolant, is not an option. The studies by Price, Price and Bailey, and Armstrong introduced in Section 1.1.1 (see [4]-[6]) on the use of LOX as a coolant demonstrate that it is technically feasible to use liquid oxidizers as the coolant, but there are no examples of this being done in practice.

In the absence of industry-proven regenerative cooling systems that use liquid oxidizers as the coolant, hybrid rocket developers, with a few exceptions, adopted ablative nozzle designs from solid rockets. One exception is the 1U CubeSat (100 mm cube) hybrid rocket thruster designed and patented by Eilers et al., which uses liquid nitrous oxide (N_2O) as the oxidizer and nozzle coolant in an annular plug nozzle [16]. Quigley and Lyne also recently developed and tested a 3D-printed liquid-cooled nozzle design [17]. Their demonstration of the successful use of 3D printing for the manufacture liquid-cooled hybrid rocket nozzles is invaluable, however they used water as their coolant and air as the oxidizer, meaning that the adiabatic flame temperature was much lower than in a typical hybrid rocket and regenerative cooling was not an option. Several years prior to Eilers et al.'s thruster design, Lemieux demonstrated experimentally that liquid nitrous oxide has an adequate cooling capability for small-scale hybrid rockets nozzles [18]. Most recently, Ercole et al. applied Lemieux's findings in the preliminary design of the spike for a N2O-

cooled aerospike nozzle design [19]. Kumar et al. also reported on the improved cooling capability of supercritical N_2O versus saturated N_2O in hybrid rocket applications [20], but have not made any working verification of their predictions.

Outside of these specific examples, hybrid rocket developers have been using nozzles made of carbon-based materials. In this sense, hybrid rockets greatly benefited from the extensive work on solid rockets. Unfortunately, the most common hybrid rocket-propellant combinations contain higher concentrations of oxidizing species than the typical solid rocket, amplifying the severity of chemical nozzle erosion. Bianchi and Nasuti show this in a numerical investigation of graphite nozzle erosion under common hybrid rocket propellant combinations, concluding that erosion rates may range from 0.05 mm/s when using N_2O as oxidizer to 0.12 mm/s when using LOX (at 1 MPa), where the erosion rate in a comparable solid rocket would be less than 0.04 mm/s [21]. The reason that the erosion rate is reduced when using N_2O as the oxidizer versus LOX, is that the presence of (inert) nitrogen in the combustion gas of N_2O and a hydrocarbon dilutes the concentrations of the oxidizing species. The mechanisms of these chemical interactions are the main topic of this research and will be discussed in detail throughout.

Before moving on, it is worth discussing regenerative, ablative and film cooling techniques as applied to the case of hybrid rockets. Figure 3 depicts a generalized hybrid rocket design with and without regenerative cooling. If regenerative cooling is not employed, a large carbon-based nozzle insert is necessary to allow for chemical erosion to take place. If regenerative cooling is employed in the traditional sense, the nozzle wall will be made of tubular channels for oxidizer to flow through, and the interface at the nozzle throat will be a high-conductivity metal, such as (oxygen-free) copper, which is labeled

"R.C.N. Type II," R.C.N. being short for "regeneratively cooled nozzle," in Figure 3. The nozzle throat design labeled "R.C.N. Type I" is a combination of regenerative and ablative cooling. This type of cooling has not been introduced in open literature, but seems like an appropriate compromise if the oxidizer fails to match the cooling performance of liquid rocket fuels. Film cooling by a cool burning insulator can be applied to either case as is shown in the figure. Given that film cooling techniques have been applied to both liquid and solid rockets in the past, it is reasonable to expect that similar techniques will be viable for hybrid rockets as well.

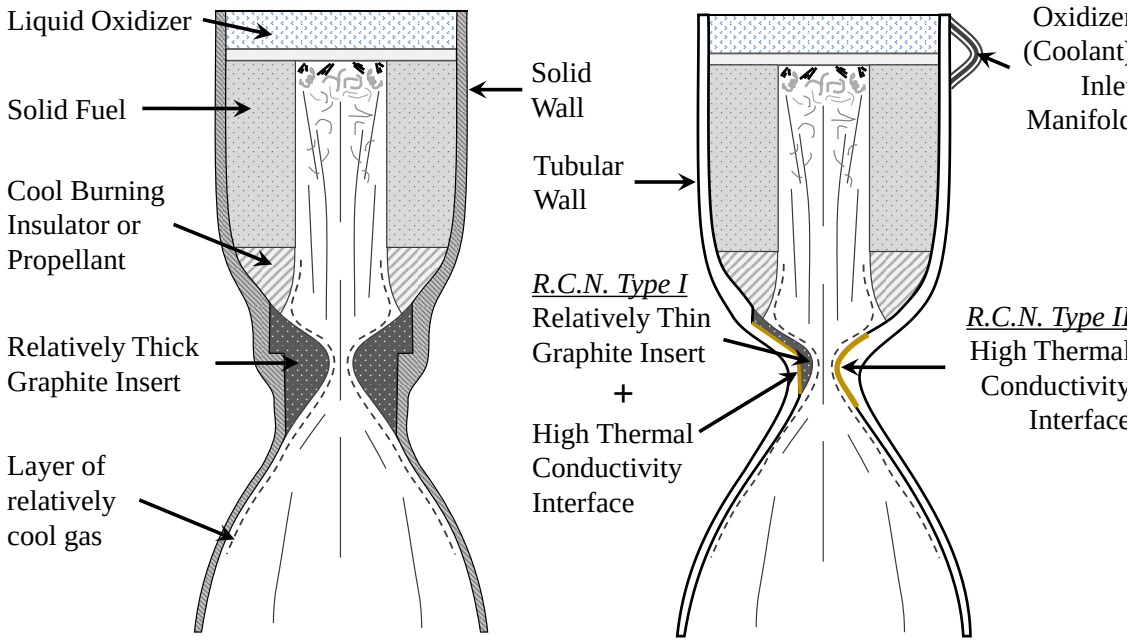

Figure 3. Thermal management concepts for (left) uncooled hybrid rocket nozzle, (right) regeneratively cooled hybrid rocket nozzles.

1.2 Impact of Nozzle Erosion on Rocket Performance

For a given propellant flow rate, $\dot{m}$ kg/s, and characteristic exhaust velocity, c^* m/s, nozzle throat erosion, i.e. an increase in the nozzle throat cross-sectional area, A_t m^2, results in a decrease in chamber pressure, P_c Pa. Characteristic exhaust velocity, c^* m/s, is the velocity that the exhaust gas would have if the nozzle had no diverging section and the gas exited perfectly perpendicularly from the nozzle throat with no heat loss to the surroundings. The momentum balance that describes c^* is depicted in Figure 4, and captured by Eq. (1-1):

$$P_c = \dot{m}c^* / A_t \tag{1-1}$$

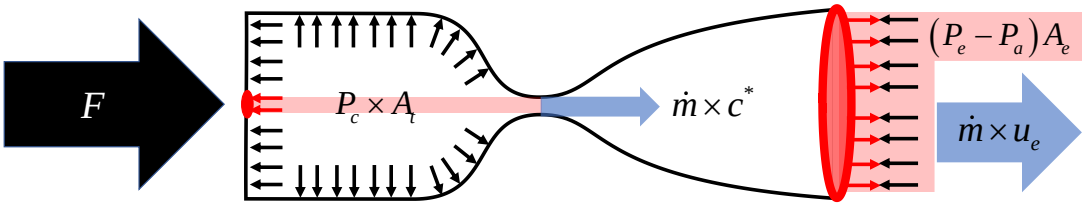

Figure 4. Momentum balance of a rocket nozzle. ***pressure forces in red and momentum forces in blue*.**

It is important to point out that the theoretical value for c^* is a function of the combustion gas constant, R J/kg-K, (stagnation) chamber temperature, T_c K, and specific heat ratio, γ, according to Eq (1-2):

$$c_{th}^{*} = \sqrt{\frac{RT_c}{\gamma}\left(\frac{\gamma+1}{2}\right)^{\frac{\gamma+1}{\gamma-1}}} = CEA\left(\xi, P_c\right) \approx CEA\left(\xi\right) \tag{1-2}$$

where the subscript "th" designates this as a "theoretical" value for c^*. The combustion gas properties R, T_c, and γ are determined by the chemical equilibrium composition of combustion gas. In this research, chemical equilibrium calculations are carried out using the NASA Chemical Equilibrium with Applications computer program, denoted by *CEA* in Eq. (1-2) [22]. The dependency of the equilibrium composition of the combustion gas on P_c is negligibly small, meaning that the decrease in P_c that results from nozzle erosion does not directly cause a change in c^*. The thrust, F N, will be affected by the decrease in P_c and reduction in the expansion ratio of the nozzle, ε, which is the ratio of nozzle exit area, A_e m^2, to the nozzle throat area. The momentum balance that describes F is also depicted in Figure 4, and captured by Eq (1-3):

$$F = \lambda \dot{m} u_e + \left(P_e - P_a\right) A_e \tag{1-3}$$

where λ is an empirical correction factor that accounts for non-isentropicity of gas expansion in the diverging section of the nozzle, as well as the axial-direction momentum losses due to friction and two-dimensional flow of gas at the nozzle exit. The term P_e is the nozzle exit pressure in Pa, and the term P_a is the surrounding atmospheric pressure in Pa. In a vacuum P_a is zero. The term u_e is the nozzle exit velocity in m/s, and is determined by Eq. (1-4):

$$u_e = c^* \sqrt{\frac{2\gamma^2}{\gamma-1}\left(\frac{2}{\gamma+1}\right)^{\frac{\gamma+1}{\gamma-1}}\left(1-\left(\frac{P_e}{P_c}\right)^{\frac{\gamma-1}{\gamma}}\right)} \tag{1-4}$$

The nozzle exit pressure is a function of ε according to Eq. (1-4):

$$\left(\frac{P_e}{P_c}\right)^{\frac{1}{\gamma}}\left(\frac{\gamma+1}{2}\right)^{\frac{1}{\gamma-1}}\sqrt{\frac{\gamma+1}{\gamma-1}\left(1-\left(\frac{P_e}{P_c}\right)^{\frac{\gamma-1}{\gamma}}\right)} = \frac{1}{\varepsilon} = \frac{A_t}{A_e} \tag{1-5}$$

To gain an understanding of the effect that nozzle erosion on the nominal performance of a rocket, it is important to consider the secondary effects of the P_c decrease (that results from erosion according to Eq. (1-1)) on the propellant mass consumption rate $\dot{m}$. These secondary effects depend on the type of rocket under consideration. Three representative cases are introduced in Table 1: a solid rocket motor (SRM), axial-injection end-burning (AIEB) hybrid rocket motor, and a conventional hybrid rocket (HRM). If we assume values for λ, P_a, and A_e of 1, 0 Pa, and 0.00785 m^2, respectively, and a nozzle throat erosion rate, $\dot{r}_t$ of 0.00005 m/s (i.e. 0.05 mm/s), we can solve the system of equations (1-1) to (1-5) and numerically integrate for nozzle throat diameter, d_t m, in time.

The results for specific impulse, I_{sp} s, and P_c for a 100 s burn are plotted in Figure 5. In all three cases nozzle erosion leads to decreases in P_c and I_{sp}, both of which are detrimental to the success of a chemical rocket. However, the severity of the performance decrease varies between cases. The SRM has the smallest percentage decrease in I_{sp} at just under 3% the initial value, but the largest decrease in P_c at more than 80%. In the SRM, any decrease in I_{sp} is solely the result of a decrease in the effectiveness of the expansion of

gas beyond the nozzle throat because ξ (i.e. c^*) is fixed. The HRM has just over a 3% decrease in I_{sp}, less than 1% larger than the SRM, and had the smallest decrease in P_c at 45%. The slightly larger loss in I_{sp} than in the SRM case is due to a slight shift in ξ away from the optimum value. In a conventional HRM, the oxidizer mass flow rate, $\dot{m}_{ox}$ kg/s, depends on the pressure drop across the injector, which will increase with a decrease in P_c due to nozzle erosion. Thus, erosion leads to a larger $\dot{m}_{ox}$, which in turn leads to a recovery of P_c, and increase in fuel mass consumption, $\dot{m}_{fu}$ kg/s. The AIEB has the largest decrease in I_{sp} at 24%, due to the large deviation from the optimal ξ. In the AIEB, the oxidizer is a choked flow, meaning that erosion will not lead an increase in $\dot{m}_{ox}$. When $\dot{m}_{fu}$ decreases due to a decrease in P_c, the value of ξ increases by the inverse of that decrease. Overall, the conventional hybrid rocket fairs the best in the face of nozzle erosion.

Table 1. Propellant mass flow rate dependencies on P_c for plots in Figure 5.

Figure 5 Designation	Description	Mass Flow Rate Dependencies*	Equilibrium Gas Properties**
SRM	Constant burning surface area (e.g. star grain) solid rocket	$\dot{m} = aP_c^n$ $= \left(2.52\times10^{-5}\right)P_c^{0.6}$	$\gamma, c^* =$ constant $\rightarrow 1.2,\ 1600$ m/s
AIEB	Axial-injection End-burning hybrid rocket. Oxidizer: GOX Fuel: Polyethylene	$\dot{m}_{fu} = aP_c^n$ $= \left(1.36\times10^{-8}\right)P_c$ $\dot{m}_{ox} =$ constant $= 0.1794$ kg/s	$\gamma, c^* = CEA\left(\xi, P_c\right)$ $CEA\left(2, 6\text{ MPa}\right)$ $\rightarrow 1.18,\ 1781$ m/s
HRM	Conventional hybrid rocket: Oxidizer: LOX Fuel: Polyethylene	$\dot{m}_{fu} = a\dot{m}_{ox}^n$ $= \left(0.322\right)\dot{m}_{ox}^{0.8}$ $\dot{m}_{ox} = c_v\sqrt{P_{up} - P_c}$ $= \left(0.322\right)\sqrt{10^7 - P_c}$	$CEA\left(3, 6\text{ MPa}\right)$ $\rightarrow 1.13,\ 1759$ m/s $CEA\left(4, 6\text{ MPa}\right)$ $\rightarrow 1.13,\ 1671$ m/s

* $\dot{m} = \dot{m}_{fu} + \dot{m}_{ox}$, where subscripts "fu" and "ox" stand for "fuel" "oxidizer"

** $\xi = \dot{m}_{ox}/\dot{m}_{fu}$ and c^* is taken to be the theoretical value (see Eq. (1-2))

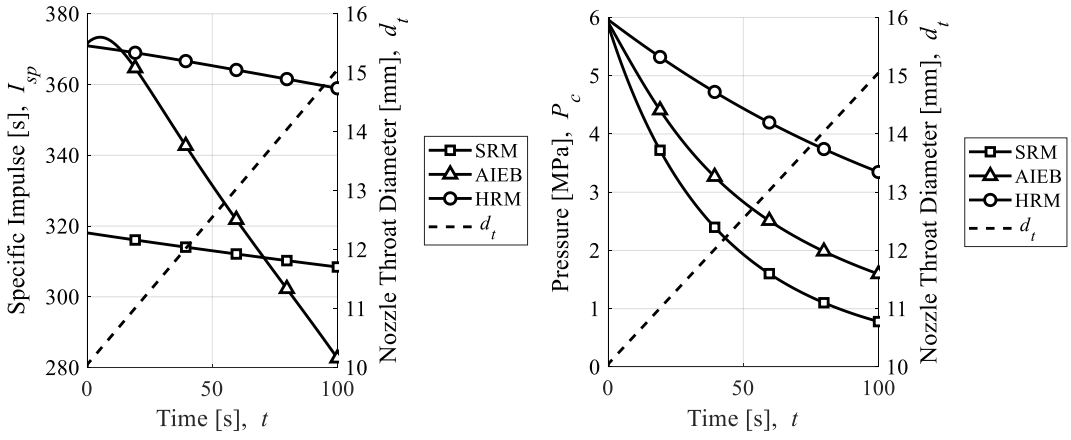

Figure 5. Effect of nozzle throat erosion on (upper) the specific impulse and (lower) the chamber pressure of three types of chemical rockets.

1.3 Review of Research on the Chemical Erosion of Graphite Nozzles

Previous research confirms that the erosion of the throat is predominantly chemical in nature, even when erosion elsewhere along the nozzle surface is mechanical. This may be inferred intuitively, because in a converging-diverging nozzle the throat is the location where the contour of the nozzle throat is parallel to the flow direction and the flow is moving near the speed of sound. Thus, even if abrasive particles exist in the combustion gas, only particles that enter the boundary layer will be driven to collide with the nozzle wall, and this collision will be not be head-on. For these reasons, chemical erosion has remained the focus of previous research, and the term "nozzle erosion" in this research will by default refer to nozzle "chemical erosion" unless otherwise specified.

The foundation of research on nozzle erosion can be thought of as starting in the mid-20^{th} century by two separate group of researchers. Meyer [23], Strickland-Constable [24][25], and Binford and Erying [26], examined the oxidation of carbon samples in chambers containing high temperature CO_2, O_2, N_2O and H_2O vapor. Their research documents the rates of oxidation in ambient conditions, and includes analysis of the Arrhenius constants for activation energy and reaction order. Roughly two decades later Delaney et al. [27], McDonald and Hedman [28], and Mayberry et al. [29] publish worked directly focused on the erosion of graphite nozzle inserts in solid rockets based on diffusion and chemical kinetic theory. In fact, the analytical model introduced in CHAPTER 2 of this thesis is essentially an extension to that of Delaney et al.'s model in [27], which in the greater context of current combustion theory would be referred to as a "one-film model," referring to [30] (pp. 532). McDonald and Hedman analyze the chemical-kinetic-limited and diffusion-limited erosion rates of graphite separately, and bridge the two with the

electrical circuit analog. Mayberry et al. carry out a purely empirical correlation based on key non-dimensional parameters from transport theory, including: Sherwood number, Sh, as non-dimensional erosion rate, Reynolds Number, Re, and Schmidt Number, Sc, as the main dependent variables, and Fourier Number, Fo, and blowing number as scaling parameters. Each of these studies shows some agreement between the model proposed and the overall nozzle erosion observed in static firing tests of solid rockets, however, the number of "knobs" that were available for adjusting the empirical model were proportionally numerous given the limited number of firing test data available for correlation.

In the 1980s, Keswani et al. [31], and Jones et al. [32], conducted experimental firing tests using solid rocket motors and reported empirical correlations of the form $\dot{r}_t \propto X_i P^n$; where the subscript X_i represents the mole fraction of oxidizing species (such as H_2O, O_2 etc.), and the pressure exponent $0.8 < n < 1$. In these reports it is not clear if the timing of the onset of erosion was predicted because time histories of the erosion progression are not postulated, but the form of the empirical correlation suggests that this is not possible. In many cases the chamber pressure reaches its design value seconds before erosion rate begins, meaning that these models would overestimate the erosion rate for these times. Borie et al. conducted three static firing tests using solid rocket motors and modeled the erosion rates according to the electrical circuit analog [33]. In their study, the progression of erosion could be inferred from the increase in throat diameter between the tests because the combustion time increased between tests and the shortest test had nearly no erosion. The electrical circuit analog captured the temperature-dependency of the Arrhenius equation which meant that times of negligibly small erosion were predicted in the

beginning of firing, however the predicted erosion onset time was earlier than the measured value.

In the 2000s, Acharya and Kuo [34], and Thakre and Yang [35], conducted numerical analysis of graphite nozzle erosion using computational fluid dynamics techniques. Acharya and Kuo reconstructed the throat erosion history of two static firing tests of different propellent compositions through measurements of pressure and thrust, and compared the results of their numerical model to these histories. They found a relatively good agreement with one solid rocket propellant, but not the other. Thakre and Yange compared their numerical predictions against Borie et al.'s results in [33], and observed a similar level of agreement to the original electrical circuit analog model, slightly overestimating the rate and timing of the onset of erosion. A few years later, Bianchi et al. conducted a detailed numerical analysis of solid rocket static firing tests conducted by Geisler et al. [36]. They conclude that the throat erosion rate of a nonmetallized propellant is predominately the result of chemical reactions with H_2O in the combustion gas. The mass fraction of H_2O, Y_{H_2O}, in the combustion gas decreased five-fold, from 15% to 3%, with only a two-fold increase, from 15% to 27%, in Al content. This decrease in Y_{H_2O} correlates with the observed decrease in erosion rate at the throat from 0.35 mm/s (for 15% Al) to 0.07 mm/s for (27% Al). Furthermore, the numerical analysis program predicted the time-averaged regression rates of five of Geisler et al.'s tests to within 4%.

The only work known to the authors that investigates graphite nozzle erosion in hybrid rocket combustion gas is a follow-on work to [36], by Bianchi and Nasuti [21]. Here, the numerical model that was validated in [36] was used to predict erosion rates for the 12

hybrid rocket propellant combinations that result from forming pairs out of the three fuels: Hydroxyl-terminated Polybutadiene (HTPB), Polyethylene (PE) and wax; and four oxidizers: oxygen (O_2), nitrogen tetroxide (N_2O_4), hydrogen peroxide (H_2O_2), and nitrous oxide (N_2O). Unlike in a solid rocket, which has a fixed propellant composition, in a hybrid rocket the oxidizer-to-fuel-mass ratio, ξ, changes in time. This makes the prediction of nozzle erosion in hybrid rocket even more demanding than in the case of solid rockets. The results of [21] greatly elucidate the major trends in chemical erosion that can be expected in hybrid rockets. First, Bianchi et al. report that erosion rates should have a global maximum in slightly oxidizer-rich conditions, in the region of equivalence ratio, $0.6 < \Phi < 1$. This is a region where adiabatic flame temperature is close to its maximum value while there is also a relatively high mass fraction of the oxidizing species CO_2, H_2O and O_2. The mass fraction of oxidizing species will continue to increase as Φ decreases, however the flame temperature will sharply decrease, driving down the erosion rate. The opposite happens with increasing Φ. The maximum flame temperature is expected in the region $1.4 < \Phi < 1.6$, but in this region the mass fraction of oxidizing species is many times lower than when $\Phi < 1$. Lastly, Bianchi et al. show that the erosion rate of any of the 12 hybrid rocket propellant combinations is greater than that expected of a conventional solid rocket propellant. The reason for this being that the mass fraction of oxidizing species is larger in the hybrid rocket propellant combustion gas. Furthermore, when O_2 is used as the oxidizer the erosion rate is expected to be roughly twice as high as that when using N_2O as the oxidizer. The erosion rates when using N_2O_4 or H_2O_2 as the oxidizer fall in between these extremes. The fuel selection is expected to have very little influence on erosion rate.

The most recent research on graphite nozzle erosion was conducted by Kamps et al. partly in collaboration with Bianchi et al. Kamps et al. developed an innovative measurement technique for determining the histories of d_t and ξ in hybrid rocket static firing tests from the commonly measured values F, P_c, $\dot{m}_{ox}$, Δm_{fu} and Δd_t [37]. The results agreed well with the prediction by Bianchi et al. in [21]. A maximum erosion rate was observed in slightly oxidizer rich conditions, and erosion rate increased linearly with chamber pressure. A joint paper in which Bianchi et al.'s numerical model was applied to Kamps et al.'s static firing tests revealed a general agreement in time-averaged erosion rates, but a disagreement in temporal changes in erosion rate. The reason for this discrepancy was most likely the result of the assumption in Bianchi et al.'s model that the nozzle temperature was steady-steady, even though, due to the short duration of firing tests conducted, the nozzle temperature was increasing rapidly in time.

1.4 The Contributions of this Research to Understanding of Nozzle Erosion

The effect that nozzle erosion has on the performance of a rocket depends on the type of rocket under consideration. In solid rockets, propellants often contain significant weight percentages of metals, such as Al, that form oxides in the combustion gas and reduce the concentration of oxidizing species, reducing the severity of thermochemical erosion. However, the impact that nozzle erosion has on performance is more pronounced, because propellant mass flow rate depends on the chamber pressure, which decreases with nozzle throat erosion. In hybrid rockets, the oxidizer is supplied to the chamber as a gas or droplet stream, and fuel is stored within the combustion chamber as a solid. The impact that nozzle

erosion has on performance is reduced because propellant mass flow rate is only partially dependent on chamber pressure, however nozzle erosion is more severe because the combustion gas tends to contain high concentrations of oxidizing species.

Small studies conducted over the past five decades have established models for predicting nozzle erosion, however the number of data and range of conditions tested for was limited. The cost of experimentation is high, and when using solid rockets to test for erosion, the range of propellant combinations that can be tested is limited by the number of experiments that can be conducted. One large discrepancy in the body of previous research is the lack of time-resolved erosion analysis. Exceptions to this are the works previously introduced as [34], as well as the doctoral work conducted by Evans [38]. The most extensive collection of time-resolved erosion histories in previous research probably belongs to Evans, who used X-ray radiography to record the throat erosion history of dozens of solid rocket firing tests. The main drawbacks of Evans' measurement technique and test apparatus were the limited scale of the tests that could be conducted due to the requirement for X-ray equipment, and the lack of nozzle temperature measurement paths. As a result, Evans' final correlation took the same form as that of Keswani et al.'s correlation in [31] and Jones et al. in [32], relating the time-averaged nozzle throat erosion rates with the mass fraction of oxidizing species and chamber pressure.

Most recently, Kamps et al. demonstrated a low-cost, highly-versatile method for conducting basic research on the mechanisms of graphite nozzle erosion through the operation of hybrid rocket test motors. The use of a hybrid rocket motor with the new measurement method means that a wide range of mixture ratios can be examined with fewer tests. Hybrid rockets are also much easier to design and manufacturer due to ease of

handling, low-toxicity and non-explosive nature of hybrid rocket fuels. The availability of time histories of all pertinent variables in the analysis previous erosion models means that numerous data points can be obtained from a single test firing. Many remaining issues have to do with the limited number of test data available, and the nearly non-existent correlation of transient heating data with what is assumed to be a chemical-kinetic limited start-up transient to nozzle throat erosion.

Thus, the knowledge gaps in our current understanding of nozzle erosion and the associated contributions expected by this research can be summarized as follows:

Knowledge Gap 1: Empirical models from previous studies fail to adequately predict the onset of erosion, or discuss the specific conditions that should be avoided to prevent chemical erosion through cooling.

Expected Contribution: Nozzle temperature histories will be determined in conjunction with erosion rate histories to quantify the activation temperature of graphite. Furthermore, tests will be conducted in which the time of shutdown is the independent variable, allowing for confirmation of the erosion onset conditions: surface features, pressure etc.

Knowledge Gap 2: There is a lack of data for erosion rate under the wide range of combustion gas compositions that are possible with hybrid rockets.

Expected Contribution: Through numerous static firing tests with hybrid rocket motors data is collected for erosion rate under a wide range of gas compositions, including combustion gas rich with molecular oxygen, or rich with unburned fuel.

Knowledge Gap 3: There is a lack of data for erosion rate in axial-injection flow fields that are found in hybrid rockets.

Expected Contribution: Three distinct flow fields will be tested: gas-phase axial-injection tubular boundary layer combustion, liquid-phase axial-injection tubular boundary layer combustion, and liquid-phase axial-injection impinging-jet boundary layer combustion.

CHAPTER 2. MODEL OF CHEMICAL EROSION

Nozzle erosion can be summarized qualitatively as a process that begins when the nozzle has reached a temperature high enough for chemical reactions to be "activated," and continues so long as the rate that new molecules are supplied to the nozzle surface matches the rate at which oxidizing species are being consumed. The key mechanisms involved in this process are depicted in Figure 6. Nozzle erosion will not occur at significant rates when the nozzle temperature is sufficiently low, even if the concentration of oxidizing species at the nozzle surface is high. The same is true when the supply of oxidizing species to the surface is sufficiently low, and the nozzle temperature high. These two extreme cases are referred to as the chemical-kinetic-limited and diffusion-limited cases, respectively.

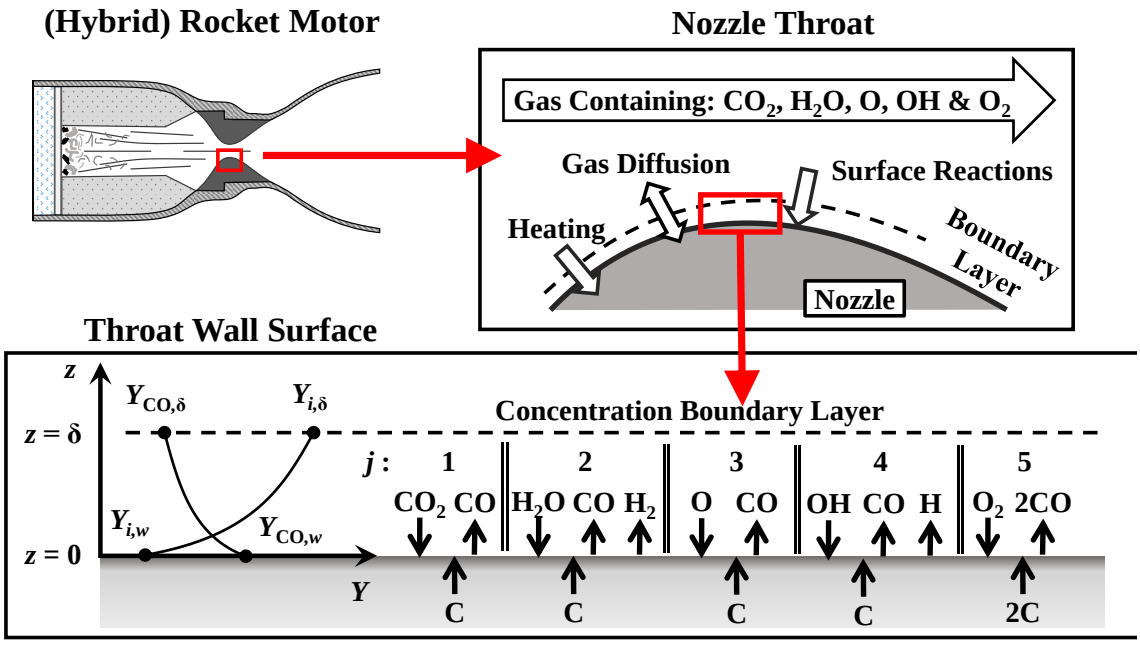

Figure 6. Oxidizing species gas diffusion at the nozzle throat during erosion.

2.1 Governing Equations of Chemical Kinetics and Mass Diffusion

Nozzle erosion is the result of heterogenous chemical reactions between the nozzle surface and the combustion gas passing over it, predominately CO_2, H_2O, O, OH and O_2. Thus, the erosion rate $\dot{r}$ at the nozzle surface can be calculated by Eq. (2-19):

$$\dot{r} = \sum \dot{r}_i \qquad i: \text{ oxidizing species} \tag{2-1}$$

Here $\dot{r}_i$ is the contribution to erosion rate from the *i*-th oxidizing species. The erosion contribution of each oxidizing species may be calculated according to an Arrhenius equation of the form in Eq. (2-2):

$$\rho_n \dot{r}_i = k_j p_i^{n_j} \qquad j: \text{ chemical reaction} \tag{2-2}$$

Here, k_j and n_j are the heterogenous rate constant and pressure exponent of the *j*-th chemical reaction, p_i is the partial pressure of species *i* at the nozzle wall, and ρ_n is the nozzle density. The rate constants are typically only a function of the nozzle wall temperature T_w, according to Eq. (2-3):

$$k_j\left(T_w\right) = A_j T_w^{b_j} \exp\left(\frac{-E_j}{R_u T_w}\right) \qquad A_j, b_j, E_j: \text{ emperical constants} \tag{2-3}$$

where R_u is the universal gas constant (R_u = 8.314 J/mol-K), and A_j, b_j and E_j are Arrhenius constants. The values for the Arrhenius constants that were reported by Bradley et al. in [39] and Chelliah in [40] are summarized in Table 2. For the reaction of O_2 with the nozzle, Eqs. (2-2) and (2-3) are not valid. The contribution of O_2 to nozzle throat erosion can be

determined by Eq. (2-4). When applying the constants in Table 2 to Eqs. (2-2) to (2-4), partial pressures should be input in units of atm, and the wall temperature in units of K.

$$\rho_n \dot{r}_{O_2} = \left(\frac{k_{5a} p_{O_2} Z}{1 + k_{5b} Z} \right) + k_{5c} p_{O_2} (1 - Z) \quad \text{where } Z = \left(1 + \frac{k_{5d}}{k_{5c} p_{O_2}} \right)^{-1} \tag{2-4}$$

Table 2. Heterogeneous rate constants and reaction order with graphite*.

Reaction**	j	ξ_j	A_j	E_j/R_u, K	b_j	n_j
$C_s + H_2O \rightarrow CO + H_2$	1	3.67	480,000	34,640	0.0	0.5
$C_s + CO_2 \rightarrow 2CO$	2	1.50	9,000	34,280	0.0	0.5
$C_s + O \rightarrow CO$	4	1.33	665.5	0.0	-0.5	1.0
$C_s + OH \rightarrow CO + H$	3	1.42	361	0.0	-0.5	1.0
$C_s + \frac{1}{2} O_2 \rightarrow CO$	5a	1.33	2,400	15,107	0.0	0.0
	5b		21.3	-2,065	0.0	0.0
	5c		0.0535	7655	0.0	0.0
	5d		18,100,000	48,845	0.0	0.0

*values taken from [39],[40].

**subscript "*s*" denotes the "solid" phase

In order to predict the nozzle erosion rates according to the Arrhenius equations described above, the partial pressure of oxidizing species at the wall must be known. The partial pressure of oxidizing species in the bulk combustion gas at the throat can be estimated through chemical equilibrium analysis, however, when nozzle erosion is taking place, oxidizing species are reacting with the wall and forming the product gas CO. Thus, a concentration gradient forms between the bulk fluid flow and the nozzle wall, and some

additional analysis is necessary to estimate the partial pressures of oxidizing species at the wall.

In the case when only the diffusion of a single oxidizing species "*i*" in the negative *z*-direction and CO in the positive *z*-direction are considered, as shown in Figure 6, the solution for surface (erosion) mass flux can be determined analytically through the integration of Fick's Law. The boundary conditions of integration are: @ $z = 0$, $Y_i = Y_{i,w}$; and @ $z = \delta$, $Y_i = Y_{i,\delta}$, as depicted in the lower left-hand side of Figure 6. The symbol Y is mass fraction, and the symbol δ is the boundary layer thickness in meters. Equation (2-5) is the solution to this integration. The derivation of similar problems can be found in [30](pp. 533-545) and in [41](pp. 551-553).

$$\rho_n \dot{r}_i = \frac{\left(\rho D_{CO,i}\right)_w}{\delta_i} \ln\left(\frac{1+Y_{i,\delta}/\xi_j}{1+Y_{i,w}/\xi_j}\right) \tag{2-5}$$

where density, ρ kg/m^3, and diffusivity, D m^2/s, were chosen to be the value of the gas mixture and binary diffusion coefficient of CO and "*i*" at the nozzle wall temperature, respectively. Similarly, the boundary condition was selected to be the concentration boundary thickness of species "*i*". The term ξ_j is the stoichiometric oxidizer-to-fuel-mass ratio of the "*j*-th" reaction – see Table 2. The binary diffusion coefficients can be predicted from the Chapman-Enskog theory. This procedure is detailed in [30](pp. 708-709). For the sake of the reader, the necessary equations and reference values will be introduced here. The governing equation for the binary diffusion constant of arbitrary gases "A" and "B" is Eq. (2-6):

$$D_{A,B} = \frac{0.0752T^{3/2}}{P\Omega\left(\sigma_A + \sigma_B\right)^2}\sqrt{\frac{1}{MW_A}+\frac{1}{MW_B}} \tag{2-6}$$

where σ Å, is hard-sphere collision diameter, *MW* kg/kmol, is molecular weight, and Ω is the dimensionless collision integral calculated according to Eq. (2-7):

$$\Omega = \frac{1.06036}{\left(T^*\right)^{0.15610}} + \frac{0.19300}{\exp\left(0.47635T^*\right)} + \frac{1.03587}{\exp\left(1.52996T^*\right)} + \frac{1.76474}{\exp\left(3.89411T^*\right)} \qquad (2\text{-}7)$$

The term T^* is a dimensionless temperature defined by Eq. (2-8):

$$T^* = \frac{T}{\sqrt{\Lambda_A \Lambda_B}} \qquad (2\text{-}8)$$

where Λ K, is the Lennard-Jones parameter. The values of σ and Λ for the gases pertinent to this research have been summarized in Table 3.

Table 3. Lennard-Jones parameters for binary diffusion coefficient calculation*.

Species	σ_i , Å	Λ_i , K	Species	σ_i , Å	Λ_i , K
Air	3.711	78.6	N_2	3.798	71.4
C_2H_4	4.163	224.7	N_2O	3.828	232.4
CO	3.690	91.7	O	3.050	106.7
CO_2	3.941	195.2	O_2	3.467	106.7
H_2O	2.641	809.1	OH	3.147	79.8

*values taken from [30].

The (concentration) boundary layer thickness of the "*i*-th" oxidizing species is estimated from the equation by Gilliland-Sherwood for diffusion of vapors into air streams in pipe flow [42], Eq (2-9):

$$\delta_i = \frac{d}{0.023\,\mathrm{Re}^{0.83}\,\mathrm{Sc}_i^{0.44}} \tag{2-9}$$

where Re is the Reynold's number of the bulk fluid flow, calculated according to Eq. (2-10):

$$\mathrm{Re} = \frac{d\rho\sqrt{\gamma RT}}{\mu} \tag{2-10}$$

and Sc_i is the Schmidt number of the "*i*-th" oxidizing species, calculated according to Eq. (2-11):

$$\mathrm{Sc}_i = \frac{\mu}{\left(\rho D_{CO,i}\right)_w} \tag{2-11}$$

2.2 Functional Dependencies of Erosion Rate

In recent years, Ozawa et al. estimated nozzle erosion rates of graphite nozzles in a computationally effective way by equating "*i*-th" erosion mass flux terms of Eqs. (2-22) and (2-5) [43]. The same procedure will be followed in this section, with the goal of identifying the key (mathematical) functional dependencies of pressure, temperature, oxidizing species concentration and scale on the overall erosion rate. Treating the reaction-diffusion balance of each species separately approximates the more complex diffusion process of the multi-component gas mixture, but it will allow for the development of an informed empirical model for experimental validation. The comparison of this simple analytical estimate of nozzle erosion rate and the experimental results of this research will

be a valuable contribution to the field. This research is the first to make a meaningful assessment of the accuracy and applicability of Ozawa et al.'s erosion rate prediction.

The values of pertinent gas properties in the combustion gas chamber can be estimated using NASA CEA and saved to a database:

$$\mu, \rho_c, T_c, R, X_i = CEA(\xi, P_c)$$

For computational purposes, the temperature, pressure and density decrease between the chamber and throat will be determined according to equations for isentropic expansion, (2-12) to (2-14):

$$P_t = \left(\frac{2}{\gamma + 1} \right)^{\frac{\gamma}{\gamma - 1}} P_c \tag{2-12}$$

$$T_t = \left(\frac{2}{\gamma + 1} \right) T_c \tag{2-13}$$

$$\rho_t = \left(\frac{\gamma + 1}{2} \right)^{\frac{1}{1-\gamma}} \rho_c \tag{2-14}$$

Here the subscript "*t*" distinguishes the bulk fluid property at the "throat," from that of "*c*" in the chamber. The density of gas close to the nozzle wall is approximated by Eq. (2-15):

$$\rho_w \cong \left(\frac{T_t}{T_w} \right) \rho_t \tag{2-15}$$

Since T_t is greater than T_w, ρ_w will be greater than ρ_t. The properties of γ, μ, R, X_i (and Y_i) are assumed to be frozen during expansion from the chamber to the throat. The mass

fraction of oxidizing species is related to the mole fraction through the relationship in Eq. (2-16):

$$Y_i = \frac{MW}{MW_i} X_i = \frac{R_u}{R} \frac{X_i}{MW_i} \tag{2-16}$$

Following Ozawa et al.'s example [43], a single implicit equation for the erosion rate can be deduced for each separate oxidizing species. The system of equations can be summarized as follows:

$$\rho_n k_j \left(\frac{MW_{mix}}{MW_i} P Y_{i,w} \right)^n = \frac{\left(\rho D_{\mathrm{CO},i}\right)_w}{\delta_i} \ln\left(\frac{1 + Y_{i,\delta}/\xi_j}{1 + Y_{i,w}/\xi_j} \right) \qquad \text{for } j\text{: 1 to 4}$$

$$\rho_n \left(\left(\frac{k_{5a} p_{\mathrm{O}_2} Z_w}{1 + k_{5b} Z_w} \right) + k_{5c} p_{\mathrm{O}_2} \left(1 - Z_w\right) \right) = \frac{\left(\rho D_{\mathrm{CO},\mathrm{O}_2}\right)_w}{\delta_{\mathrm{O}_2}} \ln\left(\frac{1 + Y_{\mathrm{O}_2,\delta}/\xi_5}{1 + Y_{\mathrm{O}_2,w}/\xi_5} \right) \qquad \text{for } j\text{: 5}$$

In each equation, the only unknown is the mass fraction of the oxidizing species at the wall, $Y_{i,w}$. Summing these equations results in the total erosion rate. This important thing to point out is that this system of equations can be solved for a given oxidizer/fuel propellant combination with just five inputs:

$$\dot{r} = f\left(d_t, P, \rho_n, T_w, \Phi\right)$$

Of these five inputs, the role of ρ_n is the least convoluted because it only appears once on the left-hand side of the equations [as in Eq. (2-2)], it's dependency is linear, and it is a constant in time. For these reasons, the four terms: d_t, P_c, T_w and Φ will be the focus of parametric analysis. The symbol Φ is equivalence ratio, and has been used instead of ξ. This representation of mixture ratio is more intuitive, because $\Phi < 1$ corresponds to the oxidizer-rich combustion, and $\Phi > 1$ corresponds to fuel-rich combustion. Of the four

independent variables under analysis (d_t, P_c, T_w and Φ), Φ is the only variable which is expected to lead to a global maximum erosion rate. In the following sections the dependencies of the other three variables will be investigated together with Φ as a two-dimensional parametric analysis. The results of this analysis are shown in Figure 7.

It is clear from Figure 7 that there are three distinct functional dependencies that emerge for d_t, P and T_w. The nozzle throat diameter exhibits a negative logarithmic functional dependency, the chamber pressure exhibits a power-law functional dependency, and the nozzle wall temperature exhibits a Sigmoid-type functional dependency. The results of curve fitting of plots in Figure 7 are summarized in Table 4. The functional dependency of erosion rate on Φ can be inferred from Table 4 because the same functional form of Φ appears in the results for all three parameters. This function is a modified form of the Gamma distribution:

$$\text{Gamma Distribution: } \mathrm{B}(\Phi) = \frac{\beta_1 \Phi^{\beta_2 - 1}}{\Gamma(\beta_2)} \exp\left(-\frac{\Phi}{\beta_3}\right)$$

The Gamma distribution, $\mathrm{B}(\Phi)$, constants β_1, β_2, and β_3 can be adjusted such that a global maximum exists, and the function tends to zero towards the origin and towards infinity. The reason that this type of functional dependency emerged from parametric analysis is clear from Figure 8, which plots the results of a detailed analysis of the Φ dependencies. The solid lines without markers represent the total erosion rate, whereas the lines with markers show the contribution to erosion rate from each oxidizing species. The dashed lines in the lower plots is the best fit of $\mathrm{B}(\Phi)$ to the total erosion rates of the upper figures.

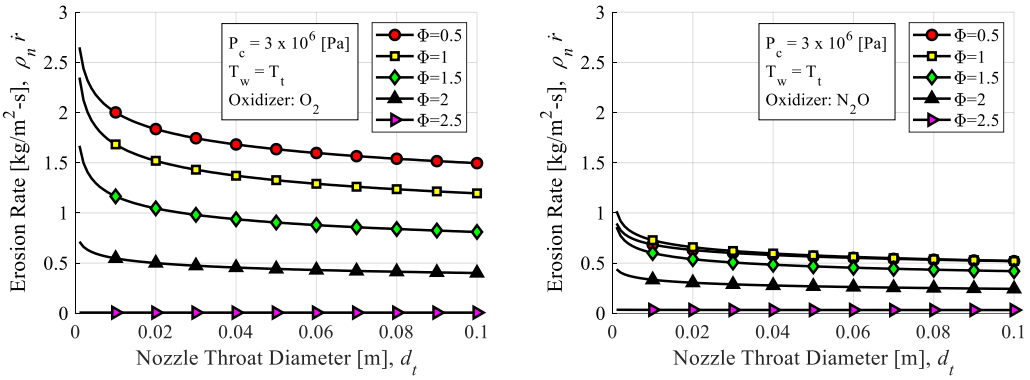

(a) Erosion rate decreases logarithmically with increasing nozzle throat diameter

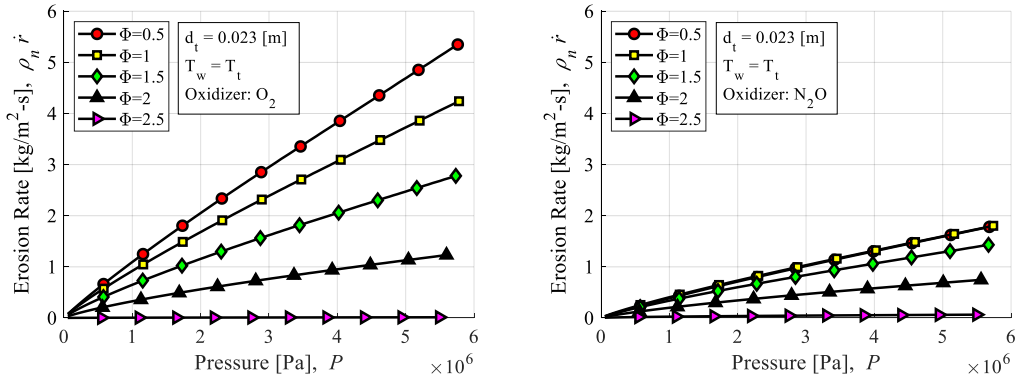

(b) Erosion rate increases nearly linearly with increasing chamber pressure

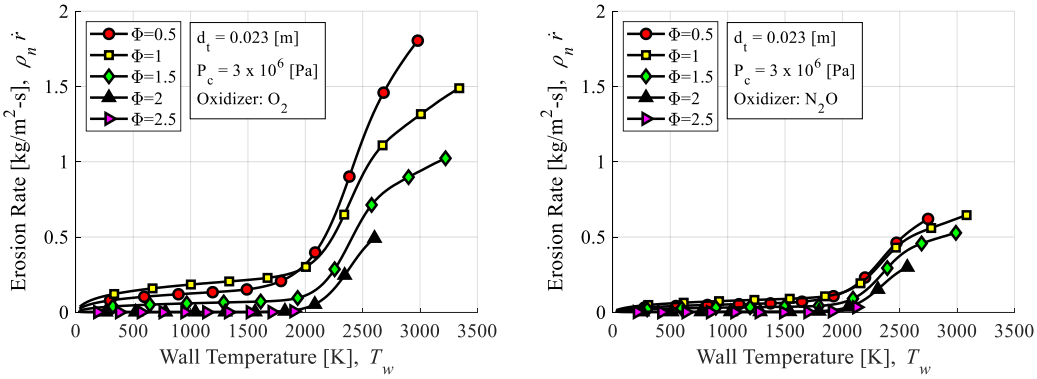

(c) Erosion is activated by a Sigmoid-type function near 2000 [K].

Figure 7. Dependencies of erosion rate on (a) d_t, (b) P_c, (c) T_w and Φ in the analytical model. *Left-hand figures for LOX/PE; right-hand figures for N2O/PE*.

Table 4. Functional dependencies of parametric analysis in Figure 7.

Parameter	Best Fit Functions for Figure 7	
	LOX/HDPE	N_2O/HDPE
d_t	$(14)\Phi^{2.6}\exp(-3.6\Phi)\left[1-\ln(d_t)\right]$	$(1.4)\Phi^{1.8}\exp(-2.2\Phi)\left[1-\ln(d_t)\right]$
P_c	$\left(2.4\times10^{-4}\right)\Phi^{2.7}\exp(-3.7\Phi)P^{0.9}$	$\left(2.1\times10^{-5}\right)\Phi^{1.8}\exp(-2.3\Phi)P^{0.9}$
T_w	$\dfrac{(0.052)\Phi^{0.6}\exp(-1.5\Phi)T_w^{0.6}}{1+\exp\left(-\dfrac{1}{180}(T_w-2320)\right)}$	$\dfrac{(0.017)\Phi^{0.7}\exp(-1.2\Phi)T_w^{0.6}}{1+\exp\left(-\dfrac{1}{170}(T_w-2280)\right)}$

The values of β_1, β_2, and β_3 from Figure 8 (c), agree well with those for the results of d_t in Table 4. Furthermore, the prediction of a maximum erosion rate in oxidizer rich conditions agrees with the findings from previous research [21][37].

Another conclusion that can be drawn from the plots in Figure 8 is that there is an obvious correlation between the magnitude of erosion rate and the mass fraction of oxidizing species. The reason that the erosion rate is larger when using O_2 as the oxidizer is larger than when using N_2O can be explained by the larger concentrations of oxidizing species. All of the subplots in Figure 7 and Figure 8 were made to have the same axis so that the difference in magnitude of erosion rate when using O_2 and N_2O would be obvious. Lastly, the reason that erosion rate does not continue to increase with increasing concentrations of oxidizing species – in the region of $\Phi < 0.5$ – is because the temperature of combustion gas sharply decreases. Gas temperature is plotted in Figure 8 (a).

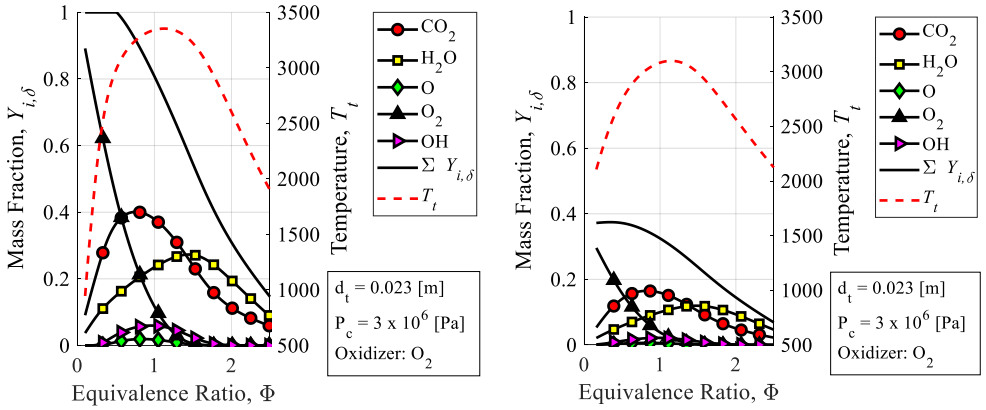

(a) The total mass fraction of oxidizing species increases with decreasing Φ

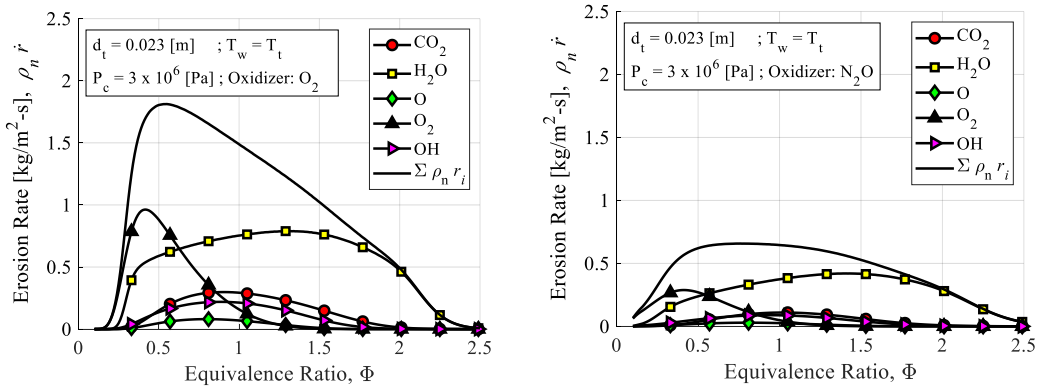

(b) Erosion rate dependency matches oxidizing mass fraction dependency in (a)

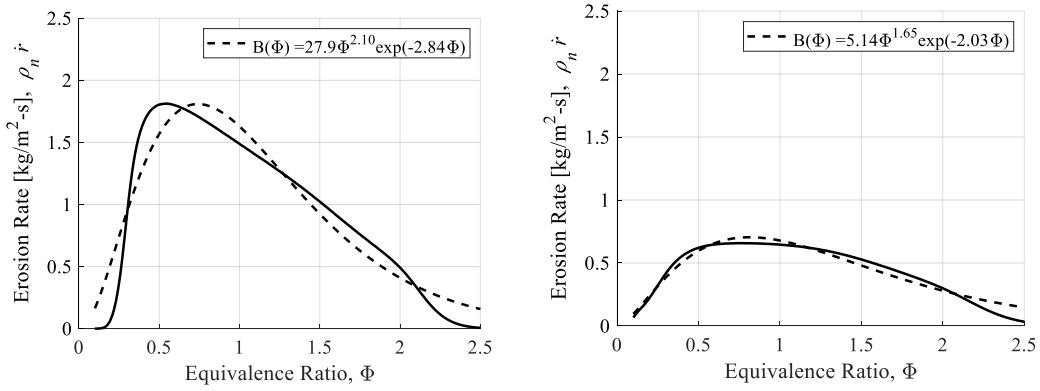

(c) Gamma distribution adequately mimics dependency of erosion rate on Φ

Figure 8. Strong dependency on concentration of oxidizing species and temperature. ***Left-hand figures for LOX/PE; right-hand figures for N2O/PE*.**

2.3 Novel Empirical Formulas

From an experimental point of view, it is not clear how to improve upon the analytical model of Section 2.2 without resorting to finding new formulations for the Arrhenius equations or mass diffusion constants from previous research. However, generalized formulas for empirical correlations can be developed based on the functional dependencies that were observed in the parametric analysis and through a qualitative understanding of the reaction-diffusion process that leads to nozzle erosion. Three models will be introduced in this section. The first is a purely mathematical interpretation of the results of Section 2.2. The second is a generalization of the circuit analogy in which the chemical and diffusion erosion rates are defined as separate conductors. The third is a modified Arrhenius equation that approximates the mass fraction of oxidizing species at the nozzle wall by a factor of mass diffusivity of oxidizing species in the bulk fluid flow. All formulas treat the combustion gas in the nozzle as a single oxidizing agent, and use a Gamma-distribution to replicate the effect of equivalence ratio on the bulk fluid behavior.

2.3.1 Formula Based on Functional Dependencies of Erosion Rate

This empirical formula is shown by Eq. (2-17):

$$\rho_n \dot{r} = \frac{\mathrm{B}(\Phi) T_w^b P^n \left[1 - \ln(d_t)\right]}{1 + \exp\left(-(T_w - E_2)/E_1\right)} \tag{2-17}$$

Where β_1, β_2, β_3, b, n, E_1 and E_2 can be determined experimentally for a give propellant combination. This empirical correlation requires data for ρ_n, $\dot{r}$, Φ, P, T_w, and d_t, however, it is clear from the analysis of Section 2.3 that the correlation should focus on the

parameters Φ, P, and T_w. The minimum number of data necessary for a statistically meaningful correlation can be surmised as follows. For β_1, β_2, and β_3 at least 5 data are needed, for b and n an additional 3 each, and for E1 and E2 at least 5: 5 (for β's), x 3 (for n) x 3 (for b) x 5 (for E's) = 225. Any set of data smaller than 225 will render at least one of the empirical constants meaningless. Increasing the statistical significance of the correlation requires even larger sets of data. For example, just increasing the number of data for each relationship by one point yields: 6 (for β's), x 4 (for n) x 4 (for b) x 6 (for E's) = 576, more than twice the minimum value.

2.3.2 Formula Based on the Electrical Circuit Analog

In the analytical model of Section 2.2, the equation of (2-2) and (2-5) leads to an implicit (transcendental) equation of $Y_{i,w}$. It is difficult to examine or interpret the transition between chemical kinetic-limited and diffusion-limited erosion regimes because of the implicit dependency on $Y_{i,w}$. Here the electrical circuit analog will be invoked to develop an alternative empirical formula to that of Eq. (2-17). The erosion rate is treated as the "current" running through a circuit consisting of two resistors. The resistors represent the inverse of the chemical kinetic-limited erosion rate and the diffusion-limited erosion rate, which can be thought of as "conductors". Therefore, the total erosion rate can be related to the chemical according to Eq. (2-18):

$$\frac{1}{\dot{r}} = \frac{1}{\dot{r}_{chemical}} + \frac{1}{\dot{r}_{diffusion}} \tag{2-18}$$

In order to form an empirical model of this circuit analog function, we must identify what components of each erosion contribution serve as fitting parameters. The strategy taken here is to treat the bulk fluid flow at the nozzle throat as a single oxidizing agent, for which we can empirical correlate the chemical kinetic rates and diffusion rates. In this way the chemical erosion contribution, $\dot{r}_{chemical}$ m/s, will be represented by an Arrhenius-type equation that is modified by a Gamma distribution to account for the dependency of Arrhenius constants of oxidizing species at the wall on the Φ. This is shown by Eq. (2-19).

$$\rho_n \dot{r}_{chemical} \cong \mathrm{B}(\Phi) T_w^b \exp\left(-\frac{E}{R_u T_w}\right)\left(P Y_\delta\right)^n \tag{2-19}$$

Here the empirical constants *b*, *E* and *n*, represent the behavior of the (bulk) oxidizing agent that is the combustion gas mixture at the throat. The mass fraction term, Y_δ, is the sum of all oxidizing species at the edge of the concentration boundary layer. In other words, when mass diffusion rates are much higher than chemical kinetic rates, we can expect that the concentration gradient across the concentration boundary layer is very small. The diffusion erosion contribution, $\dot{r}_{diffusion}$ m/s, will approximate the logarithm term (of Eq. (2-5)) by the term Y_δ / ζ, as shown in Eq. (2-20), assuming that the mass fraction of oxidizing species at the wall, $Y_w << Y_\delta$. This is valid in the diffusion-limited case.

$$\rho_n \dot{r}_{diffusion} \cong \frac{\left(\rho D\right)_w}{\delta} \frac{Y_\delta}{\zeta} \tag{2-20}$$

Substituting Eqs. (2-19) and (2-20) into Eq. (2-18) yields the empirical formula shown by Eq. (2-21):

$$\begin{aligned}\dot{r} &= \frac{\dot{r}_{diffusion}}{1+\dot{r}_{diffusion}/\dot{r}_{chemical}} \\ &\cong \frac{Y_\delta \left(\rho D\right)_w / \left(\delta \rho_n\right)}{2+Y_\delta^{1-n}\left(\rho D\right)_w \exp\left(E/\left(R_u T_w\right)\right)/\left(\delta \mathrm{B}\left(\Phi\right) T_w^b P^n\right)}\end{aligned} \tag{2-21}$$

This formula has six empirical constants: β_1, β_2, β_3 E, b and n. The exponent b may be negligibly small because the oxidizing species: CO_2, H_2O and O_2, whose sum makes up most oxidizing species over the spectrum of Φ, exhibit an exponential increase in reaction rate for all temperatures below the diffusion-limit transition, which means that b must be non-zero. For CO_2 and H_2O this is an obvious remark, because the value for b_j in Table 2 are, in fact, zero. It is also worth recognizing the resemblance of Eq. (2-21) to Eq. (2-17) in that an exponential temperature dependency function exists in the denominator, and the denominator is the sum of this term and an integer. The reason for this is that the analytical model of Section 2.2 naturally exhibits the behavior of the electrical circuit analog due to the implementation of the same general formulas for chemical kinetic-rates and diffusion rates.

One major benefit of Eq. (2-21) is that it can easily be non-dimensionalized by dividing out the diffusion mass flux term, $\left(\rho D\right)_w/\delta$, and multiplying both sides by the nozzle density, ρ_n. Another potential benefit may be the ability to apply the correlation made with one oxidizer to predict combustion using another. This is because the Gamma distribution function is isolated to the denominator, and the numerator is determined by the

mass fraction of oxidizing species rather than a Gamma distribution-type empirical formula. The non-dimensional form of Eq. (2-21) is:

$$\frac{\rho_n \delta \dot{r}}{(\rho D)_w} = \frac{Y_\delta}{2 + Y_\delta^{1-n} (\rho D)_w \exp\left(E/(R_u T_w)\right) / \left(\delta B(\Phi) T_w^b P^n\right)}$$

2.3.3 Formula Based on Modified Chemical Kinetic-Limited Erosion Rate

The results of the parametric analysis in Section 2.2 show that diffusion-limited erosion is not expected to occur until $T_w > 2750$ or so. This is because the exponent term in the denominator is larger than 0.1 for $T_w < 2750$. For temperatures larger than 2750 K, the diffusion mass flux should be the sole contributor to any further increases in temperature, for which the functional dependency is represented by the numerator of Eq. (2-17). However, it is clear from the equation for diffusion that the mass diffusivity term, $(\rho D)_w$, is strongly dependent on the wall temperature. In a paper on preliminary findings from this research, Kamps et al. showed that a modified form of the chemical erosion (Arrhenius-type) equation satisfactorily replicates the complicated reaction-diffusion behavior during nozzle erosion [44]. In this model, the mass diffusivity dependency on erosion rate in the diffusion-limited case falls on the turbulent diffusion properties in the bulk fluid flow above the concentration boundary layer, rather than on the diffusion through the boundary layer. This is done by scaling the chemical kinetic-limited erosion formula of Eq. (2-19) by the diffusion mass flux of the bulk fluid flow at the throat, $(\rho D)_t / \delta$:

$$\dot{r} = \mathrm{B}(\Phi) T_w^b \exp\left(-\frac{E}{R_u T_w}\right) (P Y_\delta)^n \frac{(\rho D)_t}{\rho_n \delta} \tag{2-22}$$

This way the erosion rate of Eq. (2-22) can be non-dimensionalized into the following empirical formula:

$$\frac{\rho_n \delta \dot{r}}{(\rho D)_t} = \mathrm{B}(\Phi) T_w^b \exp\left(-\frac{E}{R_u T_w}\right)(P Y_\delta)^n$$

In the non-dimensional form of the empirical formula, the Gamma distribution-function constant β_1 carries units that cancel out with $K^b Pa^n$.

CHAPTER 3. COMPREHENSIVE DATA REDUCTION

It was shown in Chapter 2 that it is necessary to collect hundreds of data points for $\dot{r}$, Φ, P, and T_w, for a statistically meaningful empirical correlation that can capture the complex turbulent mass diffusion and chemical-kinetic interactions of a multispecies (combustion) gas mixture and the nozzle wall. The only reasonable way to collect hundreds of data points is to measure the histories of these parameters, and ensure that some parameters change in time during a test. If a solid rocket motor were selected as the test apparatus, the value of Φ would remain constant during each test. This means that separate tests would be necessary for each data point. This is not true for a hybrid rocket motor, which has a naturally shift in Φ during firing, an in response to nozzle erosion. Furthermore, it was shown in Chapter 1 that the chamber pressure and propellant mass flow rate drop much faster in response to nozzle erosion in a solid rocket motor than in a conventional hybrid rocket motor. This means that the maximum firing durations of a solid rocket test apparatus will be restricted by the pressure loss resulting from excessive nozzle erosion. The logistical and safety costs associated with solid rocket propellant manufacturing and handling is also a limiting factor. Not only is it cheaper to conduct experiments using a hybrid rocket, but it is also safer and easier to scale up or down in size.

The main drawback to using a hybrid rocket is that determining the history of fuel mass consumption of a firing test requires some additional effort. Even in the simplest solid fuel grain designs, hybrid rocket motors are prone to a shift in Φ as the burning surface area changes during firing. The non-linear relationship between Φ, burning surface area, and solid fuel regression complicates attempts to determine the composition of gas at the

nozzle entrance. In short, it is the same complicated burning mechanisms that gives hybrid rocket motors their advantages and disadvantages for their use as experimental apparatus for conducting nozzle erosion research.

Decades of research and development on solid and hybrid rockets have led to the emergence of numerous techniques for the direct measurement of solid propellant regression [45]. These methods include but are not limited to ultrasound, x-ray radiography, microwave radiography, plasma capacitance gauge (PCG), and (embedded) resistance-based measurements. Although these techniques have been proven to be useful in certain cases, they all share a critical drawback from the perspective of this research. The first is that none of these methods is suitable for motors with complex grain geometries, which were crucial to this study. Second, except for x-ray radiography, with some tinkering and a simple fuel grain geometry, no technique is capable of measuring both the fuel regression rate and nozzle throat regression rate simultaneously using a single apparatus. Lastly, the cost-effectiveness and accuracy of employing these techniques at larger scales is either unknown or beyond consideration with the resources available for this research. There is only one category of techniques that overcomes the limitations of the others in the context of this research.

Of the multitude of measurement techniques introduced in previous research, the latest versions of the data reduction methods referred to as ballistic reconstruction techniques offer the most effective means of pursuing this research in a cost-effective and expedient way. In general, ballistic reconstruction techniques only require some combination of the following commonly measured experimental values: (1) oxidizer mass

flow rate, $\dot{m}_{ox}$; (2) chamber pressure, P_c; (3) thrust, F; (4) overall fuel mass consumed, Δm_{fu}; and (5) final nozzle throat diameter, $d_{t,f}$. This means that the same measurement equipment can be used regardless of fuel design, configuration, or scale. This is done by using either the c^* equation [Eq. (1-1)], thrust equation [Eq. (1-3)], or both, in an iterative algorithm to determine instantaneous values of the oxidizer-to-fuel mass ratio, ξ (i.e. Φ); c^* efficiency, η^* – i.e the ratio of c^*/c^*_{th}; thrust correction factor, λ; and, recently, nozzle throat area, A_t. The first ballistic reconstruction techniques were introduced by researchers Wernimont and Heister [46], and Nagata et al. [47], which used the c^* equation to determine fuel mass consumption under the assumption that η^* is constant and nozzle throat erosion does not occur. Carmicino and Sorge [48], and Nagata et al. [49], alleviated the need to treat η^* as a constant by measuring thrust and incorporating the thrust equation, but their techniques also require that nozzle throat erosion does not occur. The first technique to successfully determine the histories of nozzle throat erosion and oxidizer to fuel mass ratio with an acceptable level of uncertainty was reported by Kamps et al. [37]. Their method was titled, the "Nozzle Throat Reconstruction Technique" or "NTRT." Kamps et al., demonstrated in a follow-on study how to solve the heat equation iteratively to determine the wall temperature histories using two thermocouple measurements from within the nozzle [50]. This follow-on technique was titled the "Throat Temperature Reconstruction Technique" or "TTRT."

When operating in fuel-rich conditions, the NTRT has a range of multiple solutions. More specifically, at any given time, there may be up to three values of Φ that close the system of equations governing the NTRT. This issue existed in previous techniques as well. Nagata et al. [49]. and Saito et al. [51], made a linear approximation of the c^* in the region

of multiple solutions to overcome this issue, and showed that the loss in accuracy was acceptable in the tests under examination. Kamps et al. report than when N2O is used as the oxidizer, this region of multiple solutions is larger and more sensitive than when O2 is used, and developed an alternative to the NTRT titled, the "NTRT Plus," and labeled, $NTRT^{+}$ [52]. The concept of the $NTRT^{+}$ is to determine the fuel mass consumption history, and therefore the Φ history some other way, while still using the $NTRT^{+}$ to determine the nozzle throat erosion history. The major drawback to the $NTRT^{+}$ is that, in order to avoid multiple solutions, an alternative fuel mass consumption measurement technique must be considered. Kamps et al. suggest a simple compromise in test procedure to avoid having to incorporate any additional measurement equipment. They show that, if tests are relatively repeatable, fuel mass consumption history could be inferred from end-point data – i.e. the change in fuel mass consumption before and after firing. This is done by conducting multiple tests which start at the same initial conditions but shut down at different times. Th

Kamps et al. refer to the combination of testing and analysis through the NTRT, or $NTRT^{+}$ and the TTRT as "Comprehensive Data Reduction" [52]. The information flow of comprehensive data reduction is depicted in Figure 9. The Tiers of the operation represent places where data enters or exits a program. The left-hand side represents the original NTRT, and the right-hand side the $NTRT^{+}$. The NTRT is a Tier I operation because it can be carried out if a test has been conducted. The $NTRT^{+}$ requires multiple tests to be completed, and a time trace of fuel mass consumption to be resolved in a prior operation, which is why it is listed as a Tier II operation. However, the governing equations to all operations are the same.

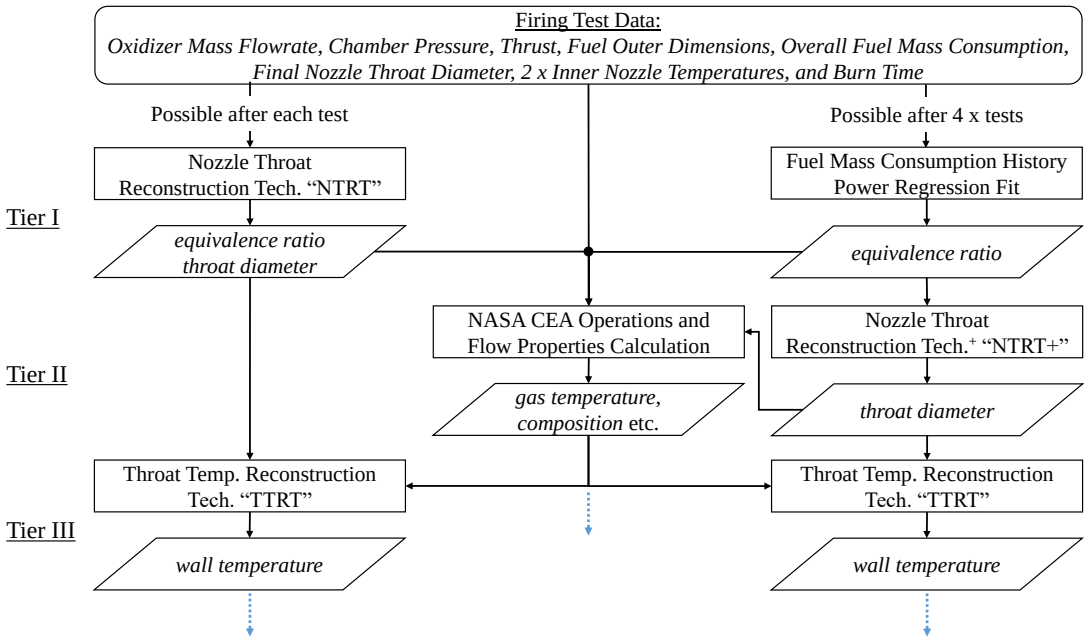

Figure 9. Flowchart of comprehensive data reduction operations in this research.

3.1 The Nozzle Throat Reconstruction Techniques

In this research, only the NTRT and NTRT+ are used to evaluate the nozzle throat erosion rate. Since both techniques have the same governing equations, they will be introduced in tandem. The calculations of each technique can be summarized by the flowchart depicted in Figure 10. The key assumptions underlying the NTRT is that η^* and λ are constants in time, whereas in the NTRT$^+$ only λ is assumed to be constant. The algorithm underlying the NTRT and NTRT$^+$ is the minimization procedure of the residual term labeled as Ψ_{NTRT}. This residual term is defined by Eq. (3-1) for both techniques.

$$\Psi_{NTRT} = \begin{cases} \sqrt{\left(1-\dfrac{\sum \dot{m}_{fu}\Delta t}{\Delta m_{fu}}\right)^2 + \left(1-\dfrac{d_t\left(t_f\right)}{d_{t,f}}\right)^2} = f\left(\lambda,\eta^*\right) & \text{for the NTRT} \quad (3\text{-}1a) \\ \sqrt{\left(1-\dfrac{d_t\left(t_f\right)}{d_{t,f}}\right)^2} = f\left(\lambda\right) & \text{for the NTRT}^+ \quad (3\text{-}1b) \end{cases}$$

The summation term under the square root sign of the NTRT residual is the numerical integration of the calculated value of fuel mass flow rate, and the term Δm_{fu} is the measured value of fuel mass consumption. The term $d_t(t_f)$ is the calculated value for final nozzle throat diameter, and $d_{t,f}$ is the measured value. The NTRT residual is the discrepancy between calculated results for overall fuel mass consumption and overall nozzle throat erosion, which is minimized through the iteration of efficiency terms, λ and η^*.

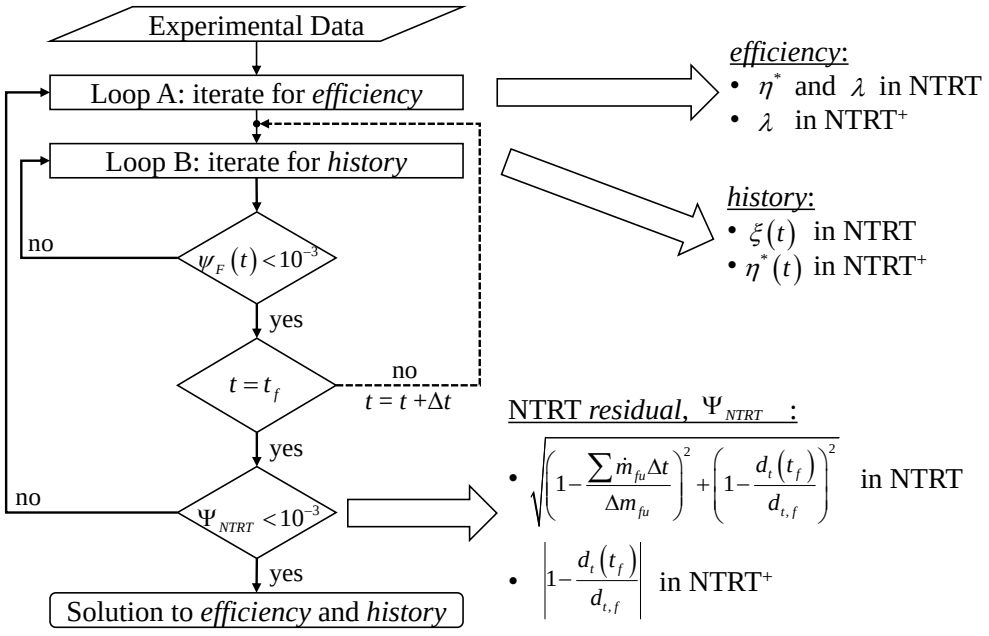

Figure 10. Flowchart of the NTRT and NTRT+ calculations.

The thrust residual term, ψ_F is essentially the same in both the NTRT and NTRT$^+$ except for which "history" is being solved for, according to Eq (3-2):

$$\psi_F(t) = \left| 1 - \frac{\lambda \dot{m}(t) u_e(t) + \left(P_e(t) - P_a\right) A_e}{F(t)} \right| = \begin{cases} f\left(\xi(t)\right) & \text{for the NTRT} \quad (3\text{-}2a) \\ f\left(\eta^*(t)\right) & \text{for the NTRT}^+ \quad (3\text{-}2b) \end{cases}$$

The NTRT solves for $\xi(t)$ while the NTRT$^+$ solves for $\eta^*(t)$ using the thrust equation. The term $F(t)$ in the denominator of Eq. (3-2) is the measured history of thrust, while the numerator is the calculated value resulting from the NTRT or NTRT$^+$ operation. Please refer to CHAPTER 1, Eqs. (1-1) to (1-5) for how to calculate specific terms within Eq. (3-2).

3.2 The Throat Temperature Reconstruction Technique

The TTRT procedure is less complicated than the NTRT or NTRT plus procedure, and similar temperature calculations have been done in previous research on rocket nozzles. Mehta reported results from a technique where the heat flux at the nozzle wall is iterated for until the temperature profile history is solved for at every time step [53]. Mehta's procedure only requires one thermocouple calculation at the boundary, making it susceptible to computational instabilities. Narsai et al. also performed a similar calculation to Mehta, and took additional thermocouple measurements to check the accuracy of the calculated profiles [54]. It is also clear from Narsai et al.'s results that the indirect calculation of nozzle temperature profiles through the iteration of wall heat flux is prone to instabilities. This means that the position and response time of thermocouples must be accurately matched to the computational stability criteria. The method referred to as TTRT

by Kamps et al. alleviates these sensitivities through the input of additional thermocouple data. Instead of iterating for wall heat mass flux, Kamps et al. iterate wall temperature. The iteration criteria is the agreement in temperature of a secondary thermocouple placed between an outer thermocouple and the wall. At every time step, t_i s, the nozzle temperature profile, T_n K, is solved for according to Eq. (3-3):

$$\begin{bmatrix} T_{w+\Delta r}^{j+1} \\ T_{w+2\Delta r}^{j+1} \\ \vdots \\ T_{r_{n,2}-2\Delta r}^{j+1} \\ T_{r_{n,2}-\Delta r}^{j+1} \end{bmatrix} = \begin{bmatrix} b_{w+\Delta r}^{j} & c_{w+\Delta r}^{j} & 0 & 0 & 0 \\ a_{w+2\Delta r}^{j} & b_{w+2\Delta r}^{j} & c_{w+2\Delta r}^{j} & 0 & 0 \\ 0 & \ddots & \ddots & \ddots & 0 \\ 0 & 0 & a_{r_{n,2}-2\Delta r}^{j} & b_{r_{n,2}-2\Delta r}^{j} & c_{r_{n,2}-2\Delta r}^{j} \\ 0 & 0 & 0 & a_{r_{n,2}-\Delta r}^{j} & b_{r_{n,2}-\Delta r}^{j} \end{bmatrix}^{-1} \left(- \begin{bmatrix} d_{w+\Delta r}^{j} T_{w+\Delta r}^{j} \\ d_{w+2\Delta r}^{j} T_{w+2\Delta r}^{j} \\ \vdots \\ d_{r_{n,2}-2\Delta r}^{j} T_{r_{n,2}-2\Delta r}^{j} \\ d_{r_{n,2}-\Delta r}^{j} T_{r_{n,2}-\Delta r}^{j} \end{bmatrix} - \begin{bmatrix} a_{w+\Delta r}^{j} T_{w}^{j} \\ 0 \\ \vdots \\ 0 \\ c_{r_{n,2}-\Delta r}^{j} T_{n,2}^{j} \end{bmatrix} \right) \tag{3-3}$$

T_w at $j+1$ — Stiffness Matrix — T_w at j — Boundary

$$\begin{aligned} a_i^j &= 2\alpha^j r_i \Delta t - \alpha \Delta r \Delta t \\ b_i^j &= -(4\alpha^j r_i \Delta t + 2 r_i \Delta r^2) \\ c_i^j &= \alpha^j \Delta r \Delta t + 2\alpha^j r_i \Delta t \\ d_i &= 2 r_i \Delta r^2 \end{aligned}$$

where Δt is a time step set to match the sampling rate of the temperature data, Δr is the radial mesh spacing, subscript i is the radial node index, and superscript j is the time index. A depiction of the radial mesh is shown in Figure 11, and the computation algorithm is depicted in Figure 12. In Eq. (3-3), the temperature profile vector at time "j+1" is the value that is being solved for, and the temperature profile vector at time "j" is the solution from the previous time step. The iteration for $T_w(t)$ ends when the inner thermocouple temperature residual, i.e. TTRT residual, $\Psi_{TTRT}(t)$ is close to zero, according to Eq. (3-4):

$$\Psi_{TTRT}(t) = \sqrt{\left(1 - \frac{T_n(r_1, t)}{T_{n,1}(t)}\right)^2} \tag{3-4}$$

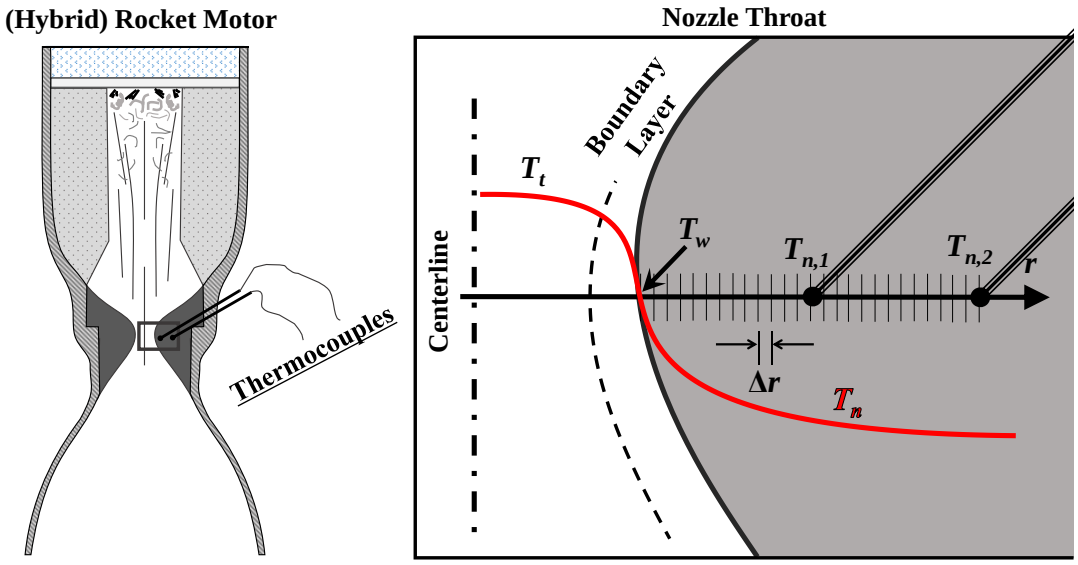

Figure 11. Radial mesh and thermocouple positions for TTRT calculations.

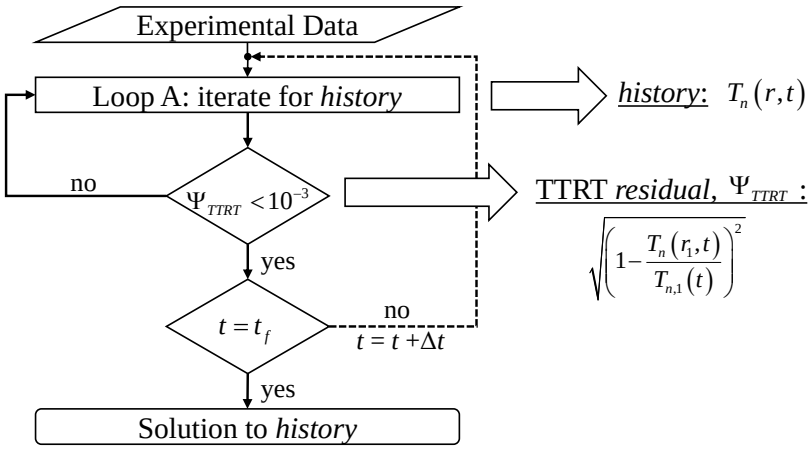

Figure 12. Flowchart of the TTRT calculations.

TTRT calculations are possible because we can assume at the beginning of combustion that entire nozzle temperature is the value of the thermocouple at position "2" (i.e. $T_{n,2}$). After this initial calculation has been completed, the solution can serve as the initial condition for the next time step.

CHAPTER 4. HYBRID ROCKET MOTOR OPERATION

Hybrid rocket static firing tests for this research were conducted continuously over the span of nearly three and a half years, from the fall of 2015 to the winter of 2018, at two separate facilities, one at the University of Hokkaido and one at Uematsu Electric Company, with teams of student members. Consequently, the test apparatus and operation procedures improved in time. The two test facilities today are far better organized and equipped to monitor and record more test data than before. Explaining these incremental improvements would be an unwarranted distraction from the main topic of study. The main objective of this chapter is to describe how the core set of measurements for employing the Comprehensive Data Reduction methods of CHAPTER 3 were obtained, and how experimental uncertainties in these measurements were quantified and/or overcome.

4.1 Experimental Apparatus

The test setup at Hokkaido University was designed to accommodate hybrid rocket motors that produce 500 N of thrust or less, although most of the tests conducted for this research had thrusts of 100 N or lower. The test setup at Uematsu Electric Company was designed to handle hybrid rocket motors that produce 30,000 N (i.e. 30 kN) of thrust or less, although most of the tests conducted for this research had thrust of 8 kN or lower. A generalized depiction of these test setups is shown in Figure 13, and screen captures of static firing tests are shown in Figure 14. Although the sizes of the test stands are not the same, both stands mount the hybrid rocket motor to a sled that is suspended on rails so that thrust can be measured using a load cell, and flowrate is always measured using an orifice plate. Both test facilities have the equipment for supplying either liquid or gaseous oxidizer

the motor. When a liquid is used as the oxidizer, the oxidizer is stored in the "liquid reservoir," which is pressurized by an inert gas – usually He but sometimes Ar. The pressurizing gas forces the liquid through a baffle and into the main feed line. When gaseous oxidizer is used, the flow is choked at the orifice to improve the accuracy of the flow rate measurement and prevent pressure instabilities. Ignition is achieved by heating the fuel with a coil of nichrome wire prior to supplying oxidizer to the motor. Shut down is achieved by cutting off the supply of oxidizer and purging the system with an inert gas, such nitrogen (N_2). If the motor and test stand are not purged with an inert gas, the fuel of the hybrid rocket motor will continue to smolder, combusting with ambient air, with oxidizer left in the feed system, or both.

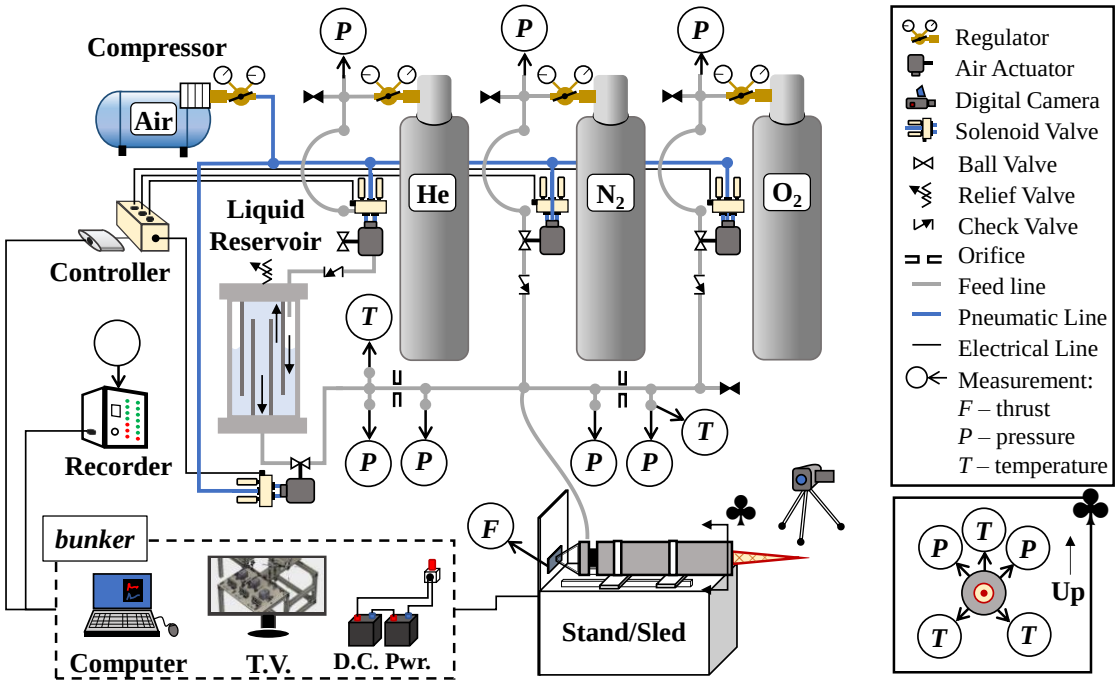

Figure 13. Generalized depiction of the test setup(s) used in this study.

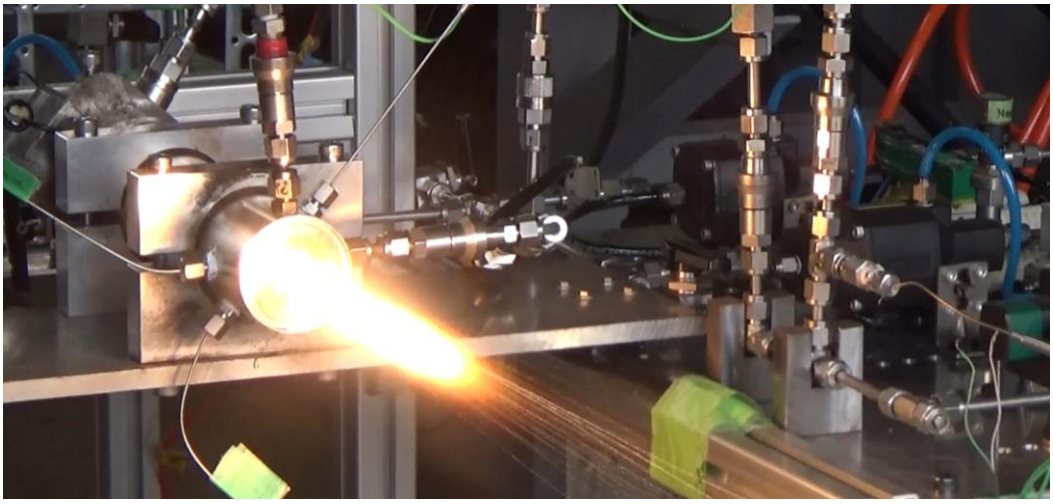

(a) Static firing test at Hokkaido University (see QE-5, CHAPTER 5)

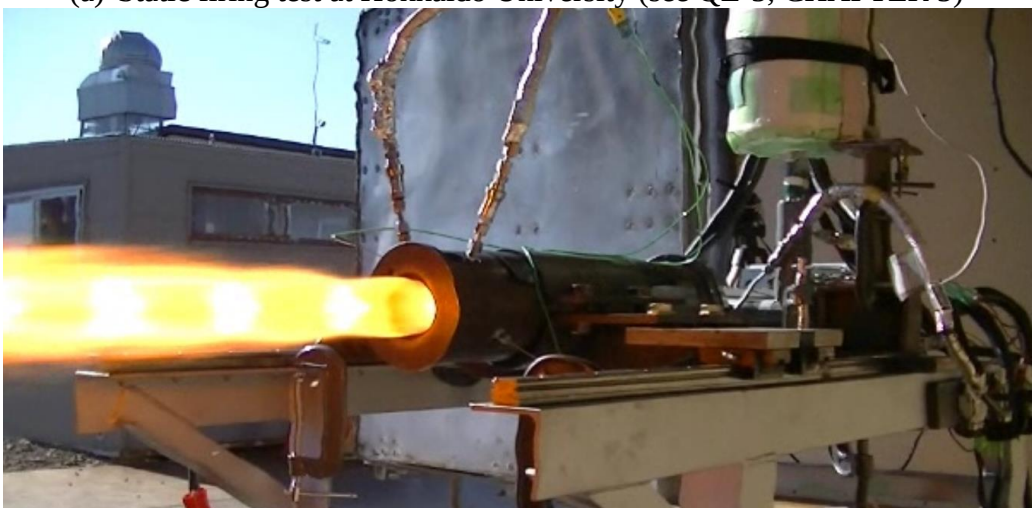

(b) Static firing test at Uematsu Electric Company (see ERM-2, CHAPTER 5)

Figure 14. Screen captures of hybrid rocket static firing tests

All tests were conducted using high-density polyethylene (HDPE | formula: C2H4 | density 955 kg/m^3) as the fuel. Tests conducted at Uematsu Electric Co. used a Cascaded Multistage Impinging-jet (CAMUI) type fuel grain, and all tests conducted at Hokkaido University used a conventional tubular fuel grain. Generally the same general hybrid rocket motor design was used for all tests conducted at Hokkaido University, where as two different designs were for tests conducted at Uematsu Electric Co. These three hybrid

rocket motors are depicted in Figure 15, Figure 16, and Figure 17, respectively. The easiest way to distinguish these designs is by geometric scale. The Hokkaido University motor, although adjustable to some degree, was roughly 60 mm in diameter and 300 mm long when assembled. The first of two designs at Uematsu Electric Co., referred to by its experiment series name, the "ERM" design is roughly twice the size of the Hokkaido University motor. When assembled the outer diameter and length were 150 mm and 600 mm, respectively. The second of two designs at Uematsu Electric Co., the "MSS" design is approximately the same length as the ERM motor, but it has twice the outer diameter, at over 300 mm when assembled. Note that the thrust class of the ERM and MSS motors is the same, 2000 N or 2 kN, thus the nozzle throat diameters are roughly the same as well.

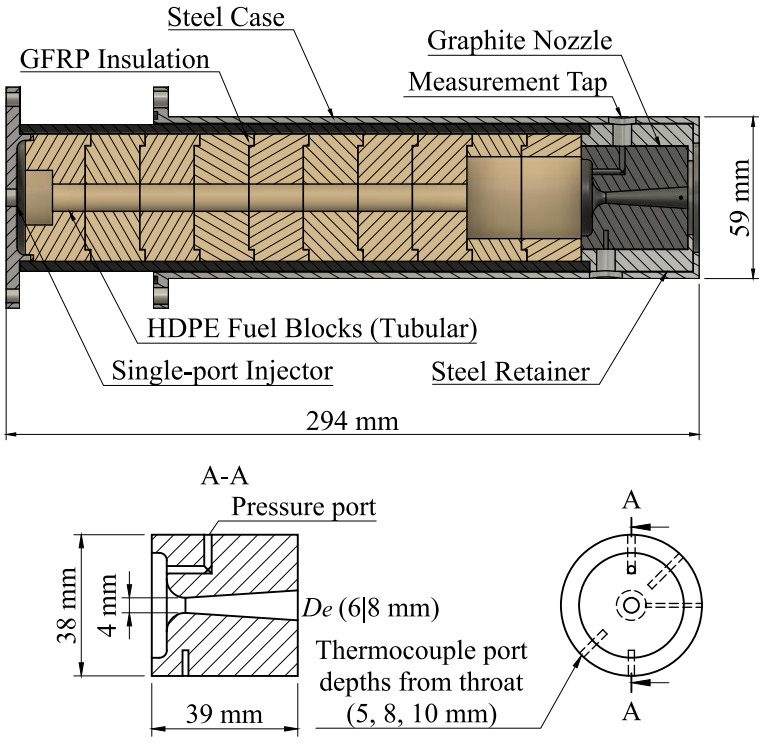

Figure 15. Hybrid rocket motor for the Hokkaido University test stand.

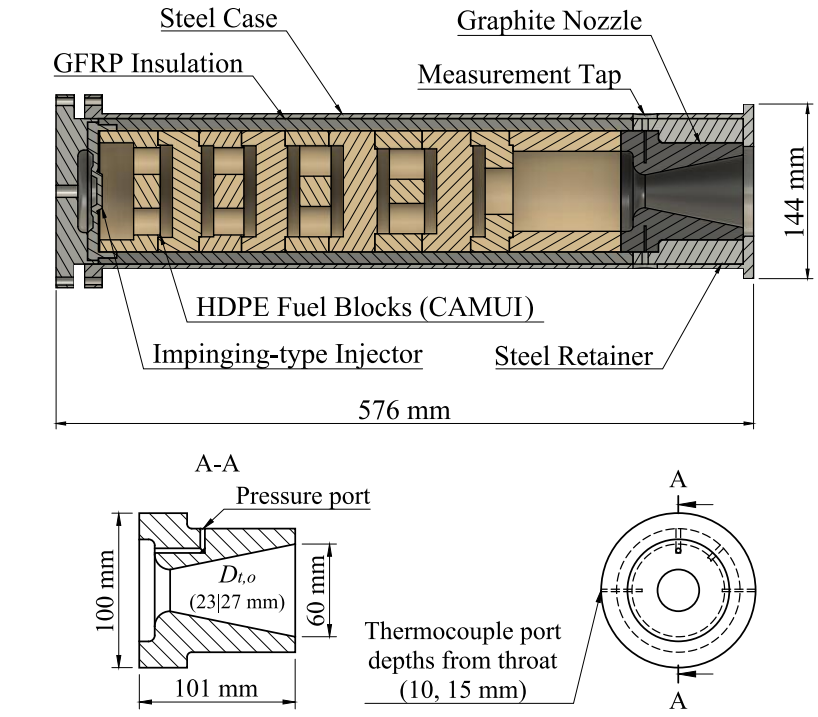

Figure 16. ERM series motor for the Uematsu Electric Company test stand.

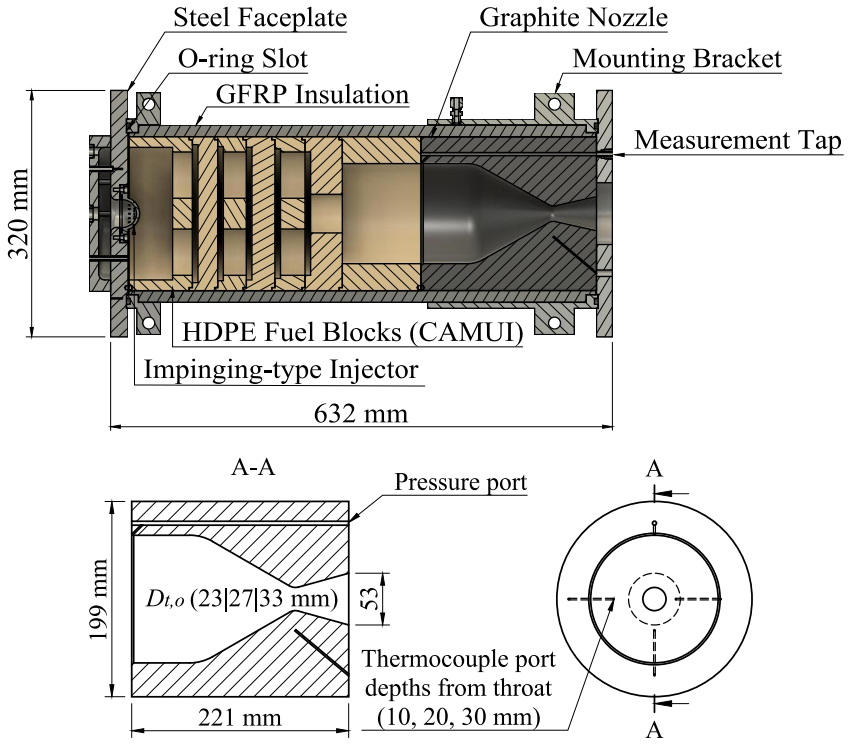

Figure 17. MSS series motor for the Uematsu Electric Company test stand.

Fuel grains in all tests were assembled from multiple short cylindrical blocks of fuel, which allowed for the correlation of fuel burning rates based on local mass flux and mixture ratio to assist in the test design process. After assembly, fuel grains were loaded into glass fiber-reinforced plastic (GFRP) insulating tubes and sealed in a steel motor case. The nozzles used in all tests were manufactured using the same grade of isotropic graphite, Tokyo Tokai Carbon Ltd. G347. The density and thermal conductivity at atmospheric conditions are listed by the manufacturer to be ρ_n = 1850 kg/m3 and k = 116 W/m-K, respectively [55]. The temperature dependency of these and other properties of G347 graphite are not specified by the manufacturer, so values were referenced from previous research on similar high-density graphite. An empirical correlation of data for thermal conductivity based on Fig. 1 in [56] yields:

$$k_n\left(T_n\right) = 3712 T_n^{-0.602} \text{ W/m-K for } 200 \text{ K} < T_n < 2500 \text{ K}$$

An empirical correlation of data for specific heat based on Fig. 1 in [57] yields:

$$c_{p,n}\left(T_n\right) = 651 \ln\left(T_n\right) - 2877 \text{ J/kg-K for } 200 \text{ K} < T_n < 3000 \text{ K}$$

4.2 Data Acquisition and Processing

As required for the NTRT and TTRT, multiple dynamic and static measurements were taken during the experiments conducted in this study. Pressures were measured using KYOWA DCS-10 MPa and KYOWA DCS-5 MPa pressure sensors with rated accuracies of ±0.040 MPa and ±0.028 MPa, respectively. In tests at Hokkaido University thrust was

measured using a KYOWA LMB-A-200N load cell with a rated accuracy of ±3.5 N, and in 2kN-thrust class tests thrust was measured using a KYOWA LCTB-A-30kN load cell with a rated accuracy of ±16 N. These instruments were calibrated by the manufacturer such that the rated accuracies account for uncertainty due to nonlinearity, hysteresis, low-temperature conditions, and external loading. Nozzle temperatures were measured using RC Pro k-type thermocouples rated up to a maximum temperature of 1100 °C with a response time of 0.3 s. Due to the low level of thrust – generally less than 100 N – produced by the Hokkaido University motors, a preload of around 50 N was applied to the injector plate using two short bungee cords (visible in Figure 14 (a)). Dynamic measurements were recorded at either 200 Hz or 1000 Hz using DCS-100A series software, and later filtered using a 20-point moving average. The reason for applying a moving average was to reduce the presence of oscillations in reconstructed nozzle throat erosion histories, which ultimately lead to undiscernible linear approximations for nozzle throat erosion rate. The uncertainty introduced by applying such moving averages is considerably smaller than the precision limits of the sensors used.

When liquid oxidizer was used, $\dot{m}_{ox}$ was calculated by the pressure drop across the orifice, ΔP Pa, according to Eq. (4-5):

$$\dot{m}_{ox} = c_d A_{or} \sqrt{2\rho\Delta P} \tag{4-1}$$

Where c_d is a dimensionless orifice discharge coefficient determined experimentally, A_{or} is the orifice cross-sectional area in m^2, and ρ is the oxidizer density upstream of the orifice. These calculations were done in a computer program so that density could be ascertained

through measurements of pressure and temperature upstream of the orifice. Formulas for the temperature dependencies of liquid N_2O and liquid O_2 density were created bas on values from the National Institute of Standards and Technology (NIST) Chemistry Webbook (liquid). The formula for liquid N_2O density, ρ_{N_2O} kg/m^3, is:

$$\rho_{N_2O}(T) = aT^6 + bT^5 + cT^4 + dT^3 + eT^2 + fT + g$$

$$\begin{aligned} a &= -6.533\times10^{-7} & e &= 0.042801 \\ b &= 3.9166\times10^{-5} & f &= -5.11433 \\ c &= -6.266\times10^{-4} & g &= 906.6779 \\ d &= -0.002521 \end{aligned}$$

And the formula for liquid O_2 density, ρ_{O_2} kg/m^3 is:

$$\rho_{O_2}(T) = 1630.7 - 5.445T$$

When gaseous oxidizer was used, the flow was choked so that $\dot{m}_{ox}$ could be calculated using Eq. (4-2):

$$\dot{m}_{ox} = c_d A_{or} P \sqrt{\left(\frac{\gamma}{RT}\right)\left(\frac{2}{\gamma+1}\right)^{\frac{\gamma+1}{\gamma-1}}} \qquad (4\text{-}2)$$

where P and T are the pressure and temperature upstream of the orifice, R is the gas constant in J/kg-K, and γ is the specific heat ratio. For gaseous oxygen stored at room temperature the terms under the square root are: T = 293 K, R = 259.8 J/kg-K, and γ = 1.395; and Eq. (4-2) reduces to:

$$\dot{m}_{ox} = 0.00248 c_d A_{or} P \quad \text{for gaseous oxygen at 293 K}$$

Initial and final throat diameter of Hokkaido University nozzles were determined using the image analysis software ImageJ [58]. An example of this process is shown in Figure 18. A photograph of the nozzle is taken from 2 meters away using 42x optical zoom. This photograph is loaded through the software ImageJ, and a length scale is set using a reference grid places next to the nozzle. The area of "particles" at the throat can be measured by making the photograph "binary" and "inverting" the black and white pixels. The nozzle throat diameter/radius is backed out of the throat area according to Eq. (4-3):

$$d_t \cong \sqrt{\frac{4}{\pi} A_d} \tag{4-3}$$

(left) setting the scale using grid paper; (right) measuring area of particles at throat

Figure 18. Throat area measurement using ImageJ (test DNT-2, CHAPTER 5).

Initial and final throat diameters of the ERM and MSS nozzles measured by hand using a Mitutoyo NTD14-20PMX digital caliper. These measurements were repeated a

minimum of 12 times, at angles of 0, 45, 90 and 135 degrees with respect to the chamber pressure measurement port. This measurement procedure is depicted in Figure 19.

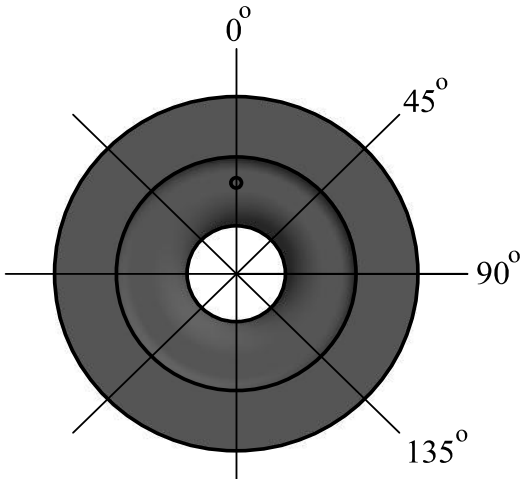

Trial	0°	45°	90°	135°
1	28.46	28.46	28.47	28.37
2	28.46	28.45	28.47	28.38
3	28.47	28.47	28.48	28.37

measurements in mm

Figure 19. Throat diameter measurement using a digital caliper (test ERM-4, CHAPTER 5)

Uncertainty in the experimental measurements of thrust, pressure etc. propagate through the NTRT, the intermediary property calculations and ultimately to the results of the TTRT. The details of this process can be summarized by Eq. (4-4), which expresses the overall uncertainty *Uy* in some NTRT/TTRT output y as a function of the inputs x_i:

$$U_y = \sqrt{\sum \left(\frac{\partial y}{\partial x_i} U_{x_i} \right)^2} \qquad (4\text{-}4)$$

where the U_{xi} terms on the right-hand side represent the uncertainty in the x_i measurement. The partial derivative terms in Eq. (4-4) represent the sensitivity of the reconstructed solution to each input. Since the algorithm in the NTRT/TTRT is a coupled non-linear problem, the partial derivative terms are approximated by Eq. (4-5):

$$\frac{\partial y}{\partial x_i} \cong \frac{y(101\%x_i) - y(100\%x_i)}{1\%x_i} \tag{4-5}$$

Here, the numerator is the change in NTRT/TTRT solution y given that the input parameter x_i has been perturbed by the amount of 1% of the nominal value.

CHAPTER 5. STATIC FIRING TEST RESULTS

A total of 60 hybrid rocket static firing tests were conducted for this research over the course of three and a half years from 2015 to 2019. The results of direct measurements necessary for carrying out comprehensive data reduction have been summarized in Table 5, and key results of comprehensive data reduction have been summarized in Table 6. These two tables were placed in APPENDIX A due to their size. Although calculations were maintained in the standard S.I. base units, the units in the tables have been selected for the ease of tabulation. Nozzle diameter, $d_{t,o}$ and $d_{t,f}$, average erosion rate, $\bar{\dot{r}}_t$, mass diffusivity D_w at the wall and boundary layer thickness, δ are listed in units of (length of) millimeters. Overall fuel mass consumption, Δm_{fu}, and average oxidizer mass flowrate, $\bar{\dot{m}}_{ox}$, are listed in units (of mass) of grams. Average chamber pressure, $\bar{P}_c$, and average throat pressure, $\bar{P}_t$ have been listed in MPa. Static firing tests can be separated into three groups: tests using gaseous oxygen (GOX) as the oxidizer, tests using liquid nitrous oxide (N_2O) as the oxidizer, and tests using liquid oxygen (LOX) as the oxidizer. These groups are sub-titled within the tables.

5.1 Comparison of Results of the NTRT and Analytical Model

Prior to this research the only readily available tool for the prediction of graphite nozzle erosion in hybrid rockets were the governing equations and calculation methodology of Delaney et al. [27] and Ozawa et al. [43] that are introduced in CHAPTER 2. This research is the first time in open literature that the accuracy and applicability of these models will be rigorously examined against static firing test results.

Since the model is indifferent to which oxidizer is used, all experimental data can be compared together. Recall that the model acts as a functional "black box", where the erosion rate is the output and the throat diameter, pressure, wall temperature, equivalence ratio and nozzle density are the inputs:

$$\dot{r} = f\left(d_t, P, \rho_n, T_w, \Phi\right)$$

The first comparison will be the simplest, the time-averaged erosion rate of all tests. These results are plotted in Figure 20. The erosion rates predicted by the model are on the same order of magnitude as the experimental values, but there is an obviously lack of correlation. In Figure 20 (left), each point represents a single test result, so the general lack of correlation between the model prediction and direct measurement means that specific tests cases are not being predicted accurately. The same is true for Figure 20 (right) as well. However, it is not particularly clear form these scatter plots what the problem is. A detailed review of specific tests will be carried out in the following sections.

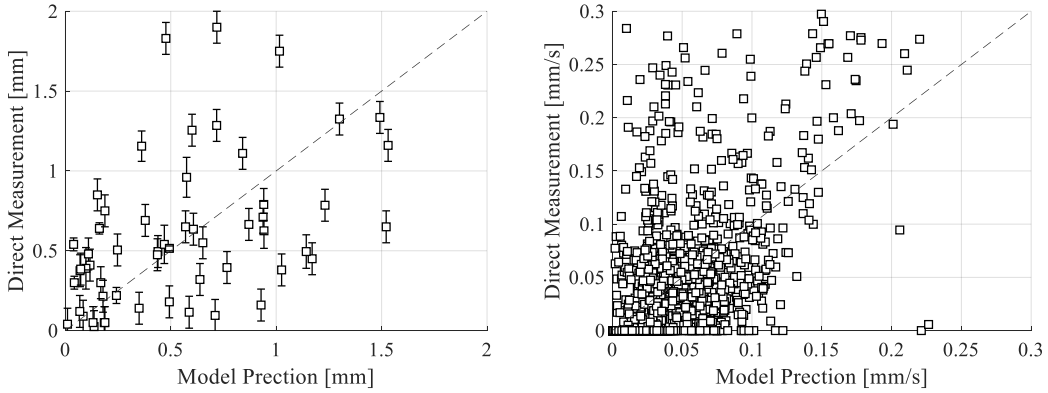

(left) overall erosion; $r_{t,f} - r_{t,o}$ (right) erosion rate at 1 s intervals

Figure 20. Poor correlation between test results and the analytical model.

5.1.1 Comparison of Measured and Predicted Erosion Histories in GOX Tests

The results of the GOX tests are broken down into five sub-groups, primarily by Series: the lower DNT-series tests, upper DNT-series tests, HK-series tests, SLY-series tests and QE-series tests. The lower DNT-series tests, i.e. DNT-3, 4, 6 & 11, and upper DNT-series, i.e. DNT-12, 13, 14, 16, 17 & 18, were conducted to test the repeatability of the NTRT and observe the progression of nozzle erosion in time. Each of these two sub-groups were tested with a fixed oxidizer mass flow rate: 11-12 g/s for the lower DNT-series; 8-9 g/s for the upper DNT-series. The results of these tests are shown in Figure 21.

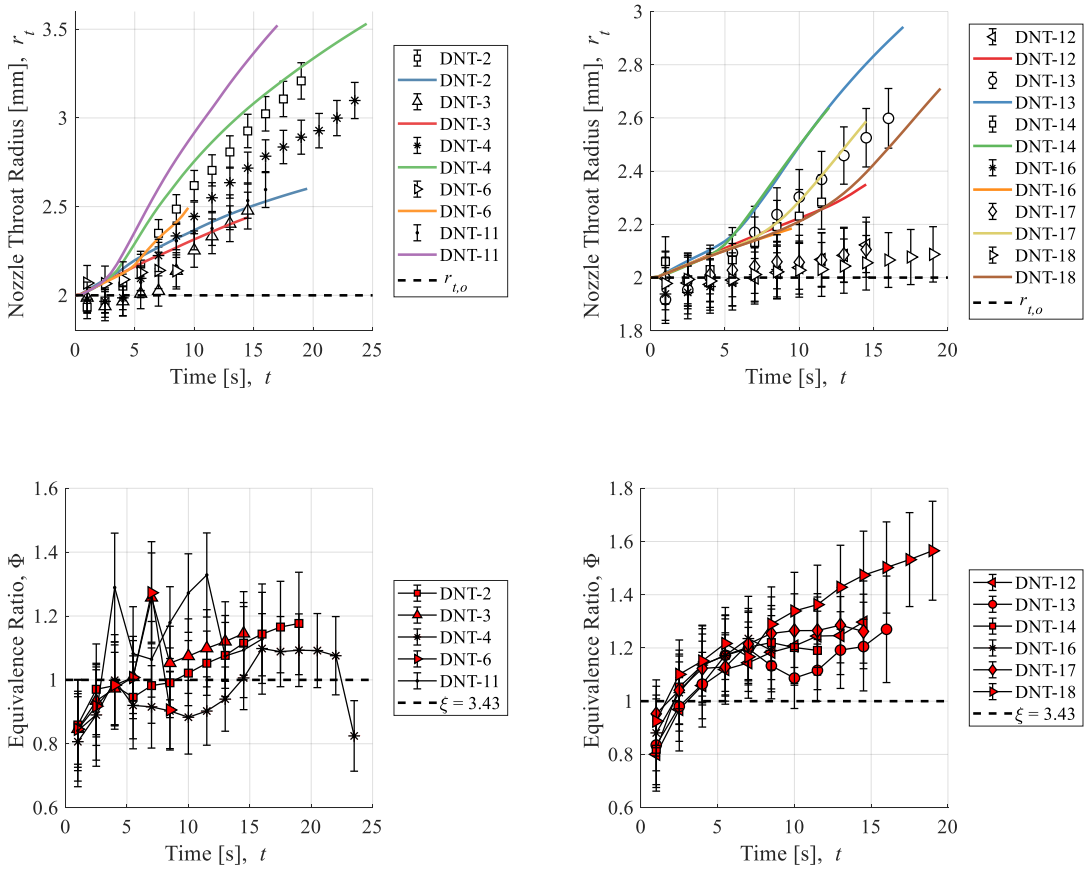

Figure 21. Model (solid lines) overpredicts measured erosion histories (markers) in lower DNT-series tests (left) and upper DNT-series tests (right).

Two conclusions may be drawn from the results of Figure 21. First, the erosion histories were repeatable in the sense that the onset of erosion and trend in erosion were consistent between tests that were shut down at different times. Second, the analytical model is able to predict roughly the correct erosion rate in tests where nozzle erosion rate is noticeably large, but unable to predict the lack of erosion observed in DNT-16 thru -18. Recognizing that the diameters, pressures and equivalence ratios are very similar between all DNT tests, the only explanation is the effect of nozzle temperature. Either the nozzle temperature measurement is consistently inaccurate, or the model cannot account for the low erosion rates observed at lower temperatures.

The results of the HK-series and SLY-series tests are shown in Figure 22. These two series have a fixed burn time of, t_b = 20 s, but varying oxidizer mass flow rates and/or fuel block configurations. The result is a large range of equivalence ratios between tests, and an equally large variation in erosion rates. In the HK-series tests, as in the DNT-series tests, the analytical model never replicates the cases where erosion rate is relatively small. This problem is not as pronounced in the SLY tests, because the erosion rates are consistently high. A careful inspection of all erosion history plots in both Figure 21 and Figure 22 reveals that although some model prediction plots line up well with an experimental measurement trace, the two plots may not be for the same test. For example, the SLY-1 model prediction in Figure 22 agrees well with the measurement history of SLY-6, whereas this predicted erosion rate is twice as high as the measured value for SLY-1.

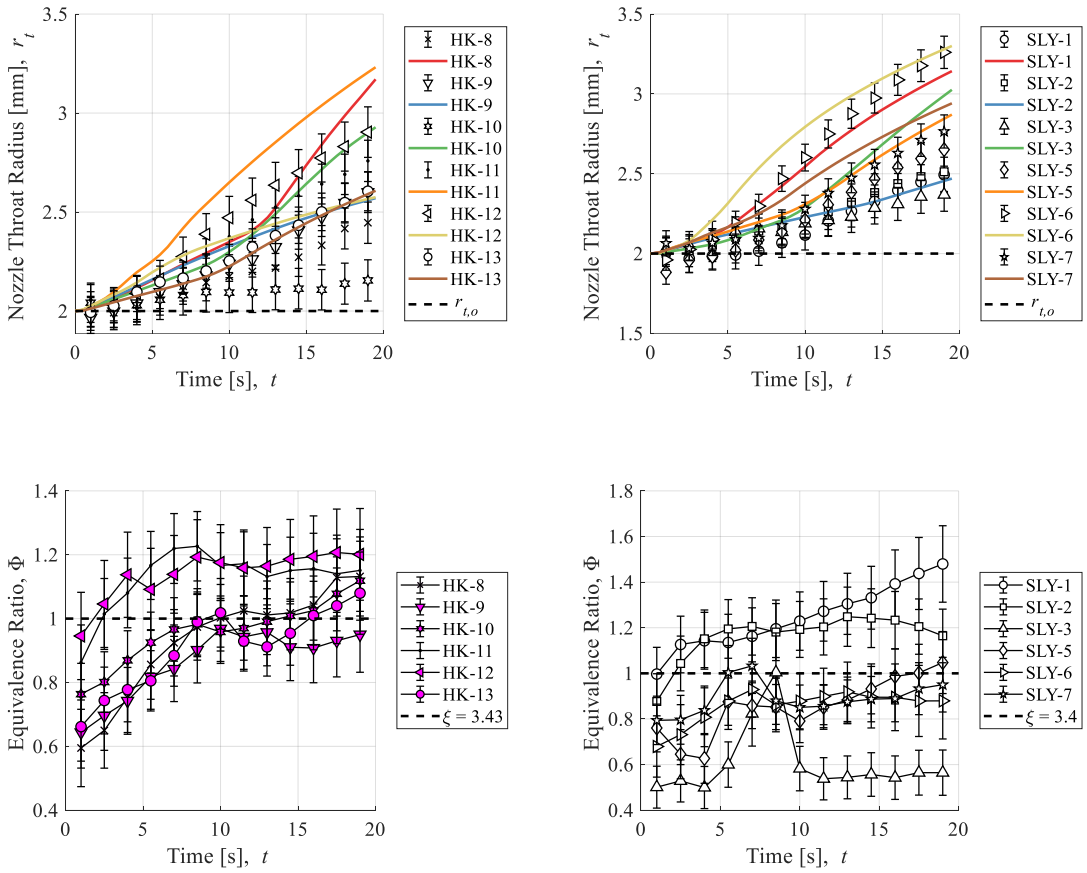

Figure 22. Model (solid lines) overpredicts measured erosion histories (markers) in HK-series tests (left) and SLY-series tests (right).

The final subgroup of GOX tests is the QE-series, which includes two DNT-series tests. These were short tests to investigate the "onset" of erosion. It was clear from the other GOX tests, which were conducted prior to the QE-series tests, that the onset of erosion is sudden, and hard to predict according to the analytical model. In the QE-series, the burn time was set to t_b = 5 s. The same fuel design and test procedures were used, and tests were conducted within days of one another to reduce the effect of environmental or human-caused experimental uncertainties. The independent variable of the QE-series tests is the oxidizer mass flow rate. This was increased by roughly 1.5 g/s across four tests, from

9 g/s to 15 g/s. Only the tests DNT-19 and QE-5, conducted at 11 g/s and 15g/s, respectively, resulted in a measurable amount of erosion with a distinct erosion onset time. The rate of erosion in QE-5, however, was nearly twice that of DNT-19. This can be explained by the combination of a higher wall temperature, higher pressure, and slightly more oxidizer rich combustion in QE-5. These tests demonstrate how particularly sensitive erosion onset is to wall temperature. The model prediction for each of these tests is roughly equivalent, consistently following the erosion history of DNT-19 in Figure 23.

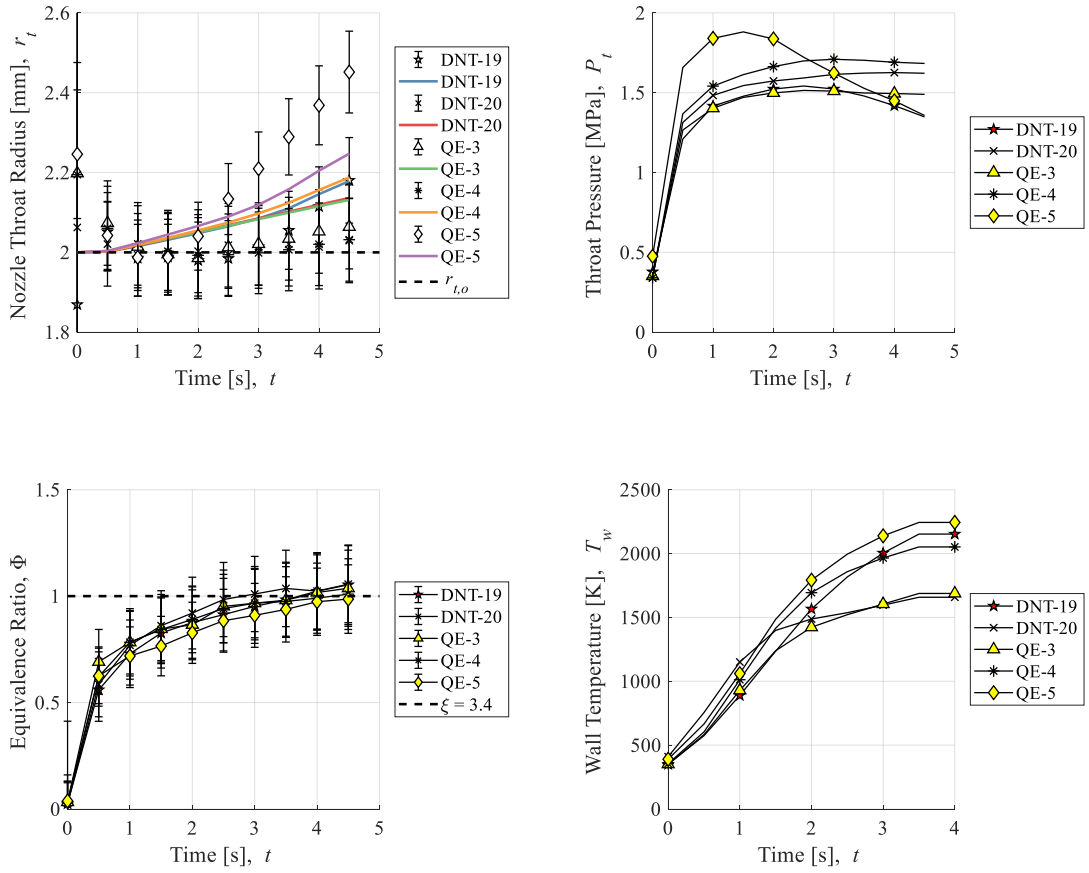

Figure 23. Erosion onset due to wall temperature and pressure in QE-series tests.

Another interesting find comes from the QE-4 test, which had negligibly small erosion, but appears to have been shut down just at the onset of erosion. Even though the nozzle erosion was not great enough to result in a significant increase in throat diameter, it can be seen from Figure 24 the throat has increased roughness and gouging similar to cases where a measurable amount of nozzle erosion has taken place.

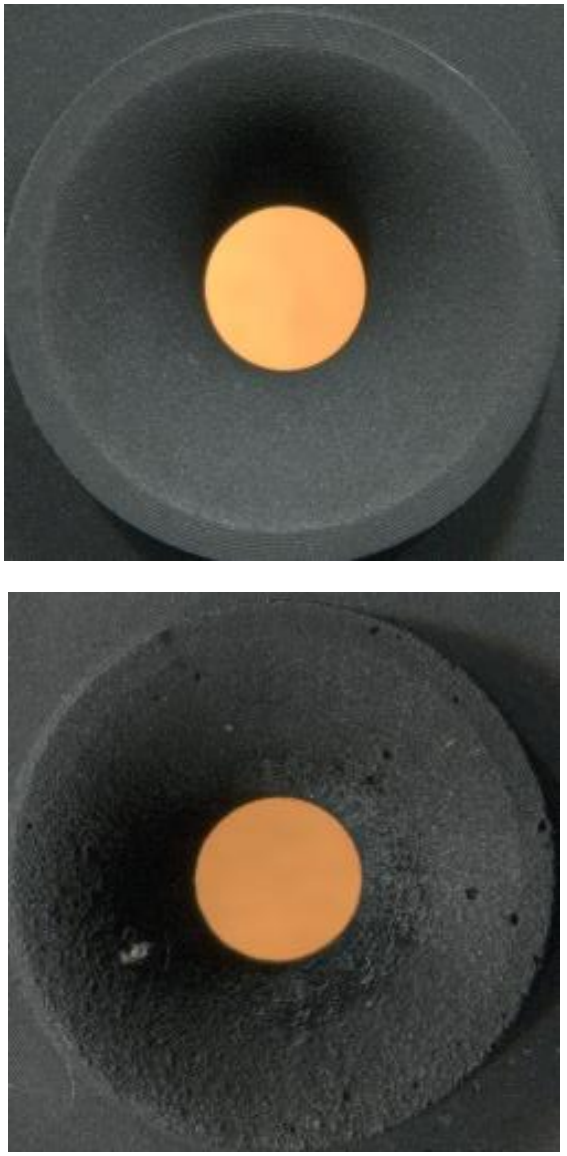

Figure 24. Increase in roughness at the nozzle throat in QE-4 before (upper) and after (lower) firing. Note: *onset appears to begin at the end of QE-4*.

5.1.2 Comparison of Measured and Predicted Erosion Histories in N_2O Tests

The results of the N_2O tests are broken down into two sub-groups of the same series: the lower CBX-series tests, and upper CBX-series tests. The lower CBX-series tests, i.e. CBX-4 thru -9, and upper CBX-series tests, i.e. CBX-10 thru -14 & 16, were conducted to test the repeatability of the $NTRT^+$ and observe the progression of nozzle erosion in time when using N_2O as the oxidizer. Initial oxidizer mass flow rate of around 40 g/, however the value increased in time in feedback to the level of nozzle erosion, as explained in Section 1.2. The fuel grain of the upper CBX-tests was shorter than the lower CBX-tests to reduce the equivalence ratio. The results of these tests are shown in Figure 25.

The influence of equivalence ratio on nozzle erosion rate is evident from Figure 25. The erosion rate of the lower CBX tests, which have an equivalence ratio between 1.6 and 2, is roughly 0.04 mm/s, whereas the erosion rate of the upper CBX tests, which have equivalence ratio between 0.8 and 1.4, is three time higher at 0.15 mm/s. The model predictions (plotted by in colored solid lines) for the CBX-series tests are just as poorly correlated, or worse, than the GOX tests. The general trends in erosion histories are similar between the model predictions and experiments, with a high erosion rate at the onset of erosion followed by a gradual decrease in erosion rate as chamber pressure decreases. However, with the exceptions of CBX-9 and CBX-14, there is poor agreement between the prediction and experimental result of any given test.

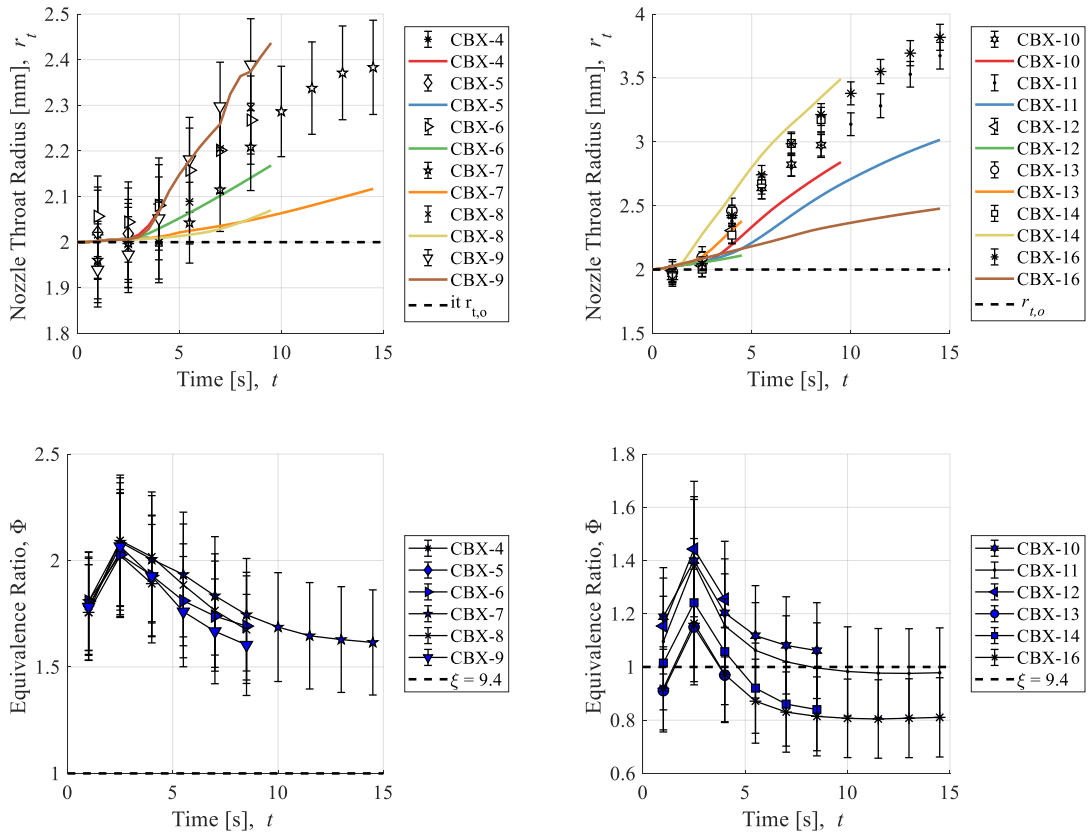

Figure 25. Model (solid lines) over/underpredict measured erosion histories (markers) in lower CBX-series tests (left) and upper CBX-series tests (right).

5.1.3 Comparison of Measured and Predicted Erosion Histories in LOX Tests

The results of the LOX tests are broken down into two sub-groups by the test series: ERM-series tests and MSS-series tests. The ERM tests were designed and carried out to examine the effect of equivalence ratio on nozzle erosion in tests using oxygen as the oxidizer. The equivalence ratio was varied by mixing fuel blocks with a conventional tubular shape with blocks that have a Cascaded Multistage Impinging-jet (CAMUI) type configuration. The CAMUI-type fuel blocks result in much high fuel consumption rates for a given oxidizer mass flow rate than a conventional tubular shape. ERM-2 and 3 burn

more fuel rich than the remaining ERM tests because they were composed mainly of CAMUI-type blocks. The MSS-2 thru -6 were carried out in a similar way to the DNT-series tests or CBX-series tests, where the combustion time was the independent variable. The MSS fuel grain design was also completely CAMUI, meaning that the fuel mass consumption as higher than most of the ERM tests. As a result, these tests burned fuel rich for long enough that the NTRT resulted in multiple solutions for a large portion of burn time. The $NTRT^{+}$ was used to determine the erosion histories to overcome this issue. The results the LOX test predictions are plotted in Figure 26.

The model predictions for erosion history are less sporadic in the LOX tests than in the GOX or N_2O tests. Furthermore, the experimental histories are consistently underpredicted by the model. It is interesting to point out that the onset of nozzle erosion is generally well predicted. This is especially clear in the MSS-2 thru -6 tests, because the experimental erosion histories show a distinct time of erosion onset at around 6 seconds in the burn, after which time erosion rate sharply increases. Although the timing of this onset is replicated, the rate of the onset of erosion and subsequent erosion rate is not. Seeing as the GOX tests were generally overpredicted, and the LOX tests underpredicted, the discrepancy in the analytical model may be an issue related to scale, such as in the Sherwood number correlation for boundary layer thickness, or effect of size and mass on the thermal properties of the nozzle etc.

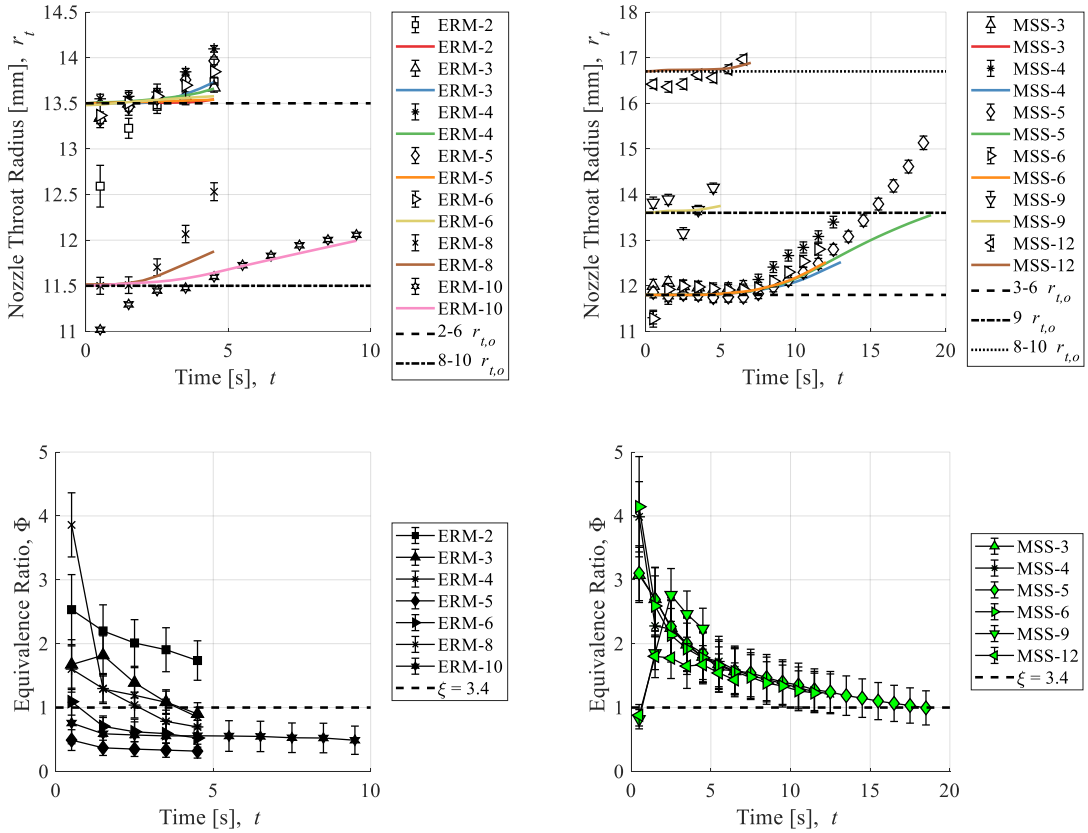

Figure 26. Model (solid lines) underpredict measured erosion histories (markers) in ERM-series tests (left) and MSS-series tests (right).

5.2 Empirical Formulation of Test Results

CHAPTER 6. IMPACT ON HYBRID ROCKET DEVELOPMENT

The main objectives of this research are to fill in knowledge gaps in chemical erosion theory, for which purpose the use of hybrid rockets were a useful tool. However, the use of hybrid rocket motors as a test apparatus comes with the consequence that a large range of combustion gas compositions tested in this study are only relevant to hybrid rocket motors. Furthermore, as discussed in Section 1.1.4, hybrid rocket engineers have the unique opportunity to combine cooling systems and technologies traditionally used in either liquid rockets OR solid rockets, but not both. Until now, there was no basis to include this kind of analysis into rocket development, because there was no data available to make an assessment of erosion, whether or not its onset can be postponed or prevented, and whether the selection of a low I_{sp} oxidizer, such as N2O, outweighs the cost of using a high I_{sp} oxidizer such as LOX that results from the increased nozzle erosion. These topics will be address in this chapter, with concluding remarks for future hybrid rocket development.

6.1 The State-of-the-Art of Hybrid Rocket Motors

Hybrid rockets are currently the focus of countless aerospace propulsion projects worldwide. Possibly the most prominent example is Virgin Galactic Ltd.'s hybrid rocket-powered spaceplane, "SpaceShipTwo", which is projected to begin commercial operations this year (FY2019) [59]. The attention on hybrid rocket development is justified by the logistical cost savings and risk reduction during operations of hybrid rockets compared to their liquid bi-propellant and solid rocket counterparts [60][14]. One potential use for the current state-of-the-art hybrid rockets is as apogee kick motors, which will alleviate satellite operators from relying solely on piggy-backing on larger satellite buses to destinations beyond geostationary transfer orbit (GTO), thus reducing launch wait times,

and increasing freedom of movement to desired orbital placements. Kuo and Chiaverini summarize the advantages of hybrid rockets for upper-stage use as having high specific impulse, throttling capability, safe manufacturing, and low cost [15](p. 632). These attributes are especially attractive when considering the application of hybrid rockets as apogee kick motors. Jens et al. reported extensively on the concept of a hybrid rocket-powered apogee kick motor for placing CubeSats into deep space [61][62][63]. Heister and Wernimont also elaborate on the practicality of hybrid rockets for space applications which demand storable oxidizers, highlighting N_2O for its low toxicity and self-pressurization ability [64].

Another potential use for hybrid rockets is as small (Earth) launch vehicles, particularly for the delivery of small payloads to LEO. Many noteworthy hybrid rocket demonstrations in recent years have been achieved. These include the aforementioned SpaceShipTwo, as well as its predecessor vehicle, SpaceShipOne [65], the highly successful Stuttgart University student-based hybrid sounding rocket, HEROS 3, reported by Kobald et al. [66], the small launch vehicles of TiSPACE Inc. reported by Chen and Wu [67], the Peregrine sounding rocket project of NASA, Stanford University, and SPG Inc. reported by Zilliac et al. [68], as well as the sounding rockets of Space Forest Ltd. reported by Gamal et al.[69]. In all of these cases, N_2O is being used as an oxidizer.

There are two distinct fuel design strategies used in the aforementioned N_2O hybrid rocket projects to achieve high thrust-to-weight ratios. One strategy is to use non-liquifying fuels with multiple ports and/or chambers to increase the burning surface area and/or create a vortex-like flow field. This is true for SpaceShipOne/Two, and the hybrid rockets reported by Chen and Wu. The other strategy is to use liquefying fuels with a single port, in which case the entrainment of liquid droplets from the surface of the melting fuel leads to high burning rates. This is true for the hybrid rockets reported by Kobald et al., Gamal et al., and Zilliac et al. In a 5 kN thrust-class sounding rocket launch reported by Nagata et

al., the former strategy was employed with great success using a high-density polyethylene (HDPE) fuel of the Cascaded Multistage Impinging-jet (CAMUI) design and liquid oxygen as the oxidizer [70]. With a characteristic exhaust velocity, c*, efficiency, η*, of 99% and a sustained acceleration during launch of 4 G to 5 G, the major concern of this development project shifted to nozzle thermochemical erosion. The tests in follow-on research to investigate nozzle erosion consistently showed values of η^* greater than 95%. Furthermore, the mass "equivalent" regression rates, based on the fuel grain outer dimensions and mass consumption rates, reached values upwards of 3 mm/s, which is comparable to or exceeding that of liquefying propellants [71]. The main drawback of using a CAMUI-type fuel, or something similar in nature, is the rigor involved in the fuel design itself. It can be said that the main benefit of using liquefying fuels in place of geometrically complex fuels, like CAMUI, is the simplicity of the single port fuel design that can be used. Mazzetti et al. make a strong argument on behalf of hybrid rockets in general, but specifically for liquefying fuel-based hybrid rockets because of the combination of the high fuel regression rate and fuel design simplicity [72].

In the context of designing an apogee kick motor, achieving a high thrust-to-weight ratio becomes less critical than in the context of a planetary launch vehicle. For example, to achieve a transfer from GTO to Mars orbit, a change in velocity of roughly 1200 m/s is required. Even at a constant acceleration of only 1 G, this apogee kick would require only a two-minute burn time. Thus, it can be said that achieving a high specific impulse, low manufacturing costs, and minimal combustion oscillations is more important in the development of an apogee kick motor than improving the fuel regression rate. In fact, Jens et al. selected the non-liquefying fuel, polymethyl methacrylate (PMMA), over a liquefying wax fuel for their hybrid rocket apogee kick motor development specifically to prevent acceleration from exceeding 3 G [63].

In the fiscal year of 2018, the Laboratory of Space Systems at Hokkaido University began the development of a hybrid rocket apogee kick motor in collaboration with the Japanese Institute of Space and Astronautical Science (JAXA/ISAS) that will be capable of transporting small satellites (less than 100 kg) from GTO to lunar orbits and beyond. Nitrous oxide (N2O) was selected to be the oxidizer for its long-term storability, non-toxicity, non-corrosiveness, low cost, widespread commercial availability, self-pressurizing ability, and successful role in the numerous projects mentioned in the previous paragraphs. High-density polyethylene (HDPE) was also selected for its non-toxicity, low cost, and widespread commercial availability, as well as for its mechanical strength and heritage in the development of the CAMUI-type hybrid rocket by the authors and their predecessors.

6.2 Design Tradeoffs of Nozzle Erosion

Concluding Remarks

6.3 Nozzle Erosion in Hybrid Rockets

Concluding remarks

APPENDIX A. TABLES OF FIRING TEST RESULTS

Table 5. Summary of Direct Measurements

Test	t_b	$d_{t,o}$	$d_{t,f}$	Δm_{fu}	$\bar{\dot{m}}_{ox}$	$\bar{P}_c$	$\bar{F}$	$\bar{T}_{n,1}$	$\bar{T}_{n,2}$	$\bar{T}_{n,3}$
	s	mm	mm	g	g/s	MPa	N	K	K	K
GOX Firing Tests (Conducted Using Hokkaido University Facilities)										
'DNT-2'	20	4.0	6.5	72	12	1.2	26	1295	1190	304
'DNT-3'	15	4.0	5.0	52	11	1.4	26	1133	1030	313
'DNT-4'	25	4.0	6.3	79	11	1.0	24	1352	1190	1109
'DNT-6'	10	4.0	4.4	33	12	1.5	25	970	765	715
'DNT-11'	17	4.0	5.3	63	11	1.4	25	1290	984	907
'DNT-12'	15	4.0	4.3	41	9	1.2	20	946		709
'DNT-13'	17	4.0	5.3	52	9	1.1	20	1230	926	896
'DNT-14'	12	4.0	4.6	34	8	1.1	19	1112	804	758
'DNT-15'	5	4.0	4.0	12	8	1.0	17	592	555	528
'DNT-16'	10	4.0	4.1	26	8	1.2	18	837	754	705
'DNT-17'	15	4.0	4.2	41	8	1.1	20	1068	843	798
'DNT-18'	20	4.0	4.2	61	8	1.2	21	1071	860	780
'DNT-19'	5	4.0	4.4	14	11	1.4	19	751	543	529
'DNT-20'	5	4.0	4.1	15	12	1.5	19	716	560	527
'DNT-21'	10	4.0	5.1	31	12	1.3	25	1103	775	769
'HK-8'	20	4.0	4.9	71	13	1.5	27	1099	1067	981
'HK-9'	20	4.0	5.3	70	14	1.4	27	1207	1141	278
'HK-10'	20	4.0	4.3	60	11	1.3	20	1090	893	810
'HK-11'	20	4.0	5.6	89	14	1.5	29	1282	1146	1116
'HK-12'	20	4.0	5.9	95	14	1.3	33	1269	1141	1080
'HK-13'	20	4.0	5.3	61	12	0.9	23	1226	1076	987
'HK-14'	20	4.0	5.4	72	13	1.1	27	1204	1189	1114
'SLY-1'	20	4.0	5.0	70	10	1.2	24	1259	977	926
'SLY-2'	20	4.0	5.1	64	10	1.1	20	1116	941	870
'SLY-3'	20	4.0	4.8	41	12	0.9	15	1178	883	817
'SLY-5'	20	4.0	5.3	57	12	1.2	22	1171	967	953
'SLY-6'	20	4.0	6.6	56	11	1.0	23	1347	1133	1056
'SLY-7'	20	4.0	5.6	59	11	1.1	23	1200	1116	1060
'QE-3'	5	4.0	4.1	14	11	1.4	24	706	584	540
'QE-4'	5	4.0	4.1	16	13	1.6	29	756	553	535
'QE-5'	5	4.0	5.0	18	15	1.6	34	833	588	578
Liquid N_2O Firing Tests (Conducted Using Hokkaido University Facilities)										
'CBX-2'	10	4.0	4.8	44	27	2.9	58	1186	965	931
'CBX-3'	5	4.0	4.2	41	39	4.2	79	809	643	583
'CBX-4'	4	4.0	4.2	35	41	4.1	78	741	588	534
'CBX-5'	4	4.0	4.1	30	41	4.1	74	661	551	519
'CBX-6'	10	4.0	4.6	74	39	4.2	81	1110	1012	960
'CBX-7'	15	4.0	4.8	110	37	4.3	88	1171	1108	1019

'CBX-8'	10	4.0	4.8	73	38	4.4	89	1003	896	823
'CBX-9'	10	4.0	5.0	74	39	4.1	83	1121	902	869
'CBX-10'	10	4.0	6.2	55	44	3.4	95	1174	975	835
'CBX-11'	15	4.0	7.5	78	47	2.9	96	848	1145	1098
'CBX-12'	5	4.0	5.0	28	42	4.0	83	748	684	614
'CBX-13'	5	4.0	5.4	23	46	4.0	86	906	790	647
'CBX-14'	10	4.0	6.7	51	46	3.4	95	1188	1053	866
'CBX-16'	15	4.0	7.7	63	48	2.8	96	1256	1217	1101
LOX Firing Tests (Conducted Using Uematsu Electric Company Facilities)										
'ERM-2'	5	27.0	27.6	1155	415	2.0	1489	630	517	-
'ERM-3'	5	27.0	27.4	999	554	2.1	1556	607	406	-
'ERM-4'	5	27.0	28.3	785	565	2.0	1523	606	525	-
'ERM-5'	5	27.0	28.1	314	628	1.3	924	570	515	-
'ERM-6'	5	27.0	27.7	499	567	1.6	1183	611	454	-
'ERM-8'	5	23.0	25.3	825	491	2.6	1492	679	540	-
'ERM-10'	10	23.0	24.0	477	310	1.3	721	827	671	-
'MSS-2'	4	23.6	23.6	1686	523	3.3	1925	502	366	321
'MSS-3'	7	23.6	24.4	2189	502	3.1	1923	673	448	367
'MSS-4'	13	23.6	27.4	3692	506	3.0	1937	929	588	454
'MSS-5'	19	23.6	30.9	4576	513	2.8	1880	1073	702	525
'MSS-6'	12	23.6	26.2	3543	504	3.1	1953	895	570	443
'MSS-8'	11	19.8	19.9	2434	324	2.7	1104	647	465	389
'MSS-9'	5	27.2	28.9	1955	627	2.9	2273	721	450	361
'MSS-12'	7	33.4	34.9	2450	729	2.2	2481	729	494	386

Table 6. Summary of Comprehensive Data Reduction Results.

Test	t_{on}	$\overline{\dot{r}_t}$	Φ	$\overline{P}_t$	$\overline{T}_{w,on}$	$\overline{\rho}_w$	$\overline{D}_w$	$\overline{\delta}$	$\overline{Y}_{ox}$	η^*
	s	mm/s		Pa	K	kg/m^3	mm^2/s	mm	K	
GOX Firing Tests (Conducted Using Hokkaido University Facilities)										
'DNT-2'	3	0.070	1.1	0.60	1954	1.0	84	0.038	0.76	0.82
'DNT-3'	7	0.060	1.1	0.80	1861	1.2	60	0.030	0.73	0.79
'DNT-4'	4	0.060	1.0	0.50	2434	0.7	138	0.046	0.80	0.78
'DNT-6'	4	0.030	1.1	0.90	2100	1.2	62	0.027	0.76	0.82
'DNT-11'	4	0.050	1.2	0.80	2696	0.8	111	0.034	0.72	0.85
'DNT-12'	7	0.020	1.2	0.70	1834	1.1	61	0.030	0.69	0.80
'DNT-13'	4.5	0.050	1.2	0.60	2564	0.7	131	0.040	0.71	0.82
'DNT-14'	3	0.030	1.2	0.70	2421	0.8	109	0.036	0.70	0.81
'DNT-15'	0	0	-	-	-	-	-	-	-	0.72
'DNT-16'	6.5	0.010	1.2	0.70	1619	1.2	52	0.031	0.68	0.77
'DNT-17'	3	0.010	1.2	0.70	2031	1.0	78	0.033	0.68	0.78
'DNT-18'	7	0.010	1.4	0.70	2179	0.9	81	0.031	0.58	0.79
'DNT-19'	2.5	0.090	1.0	0.90	1938	1.4	56	0.027	0.81	0.79
'DNT-20'	2	0.010	1.0	0.90	1556	1.8	36	0.024	0.80	0.80
'DNT-21'	2.5	0.080	1.0	0.70	2474	1.0	104	0.034	0.78	0.81
'HK-8'	2.5	0.030	1.0	0.90	2056	1.3	64	0.028	0.80	0.79
'HK-9'	2.5	0.040	0.90	0.80	1571	1.6	43	0.028	0.84	0.75
'HK-10'	2.5	0.010	1.0	0.70	1939	1.2	65	0.030	0.80	0.75
'HK-11'	3	0.050	1.2	0.80	2190	1.1	73	0.030	0.71	0.79
'HK-12'	2.5	0.060	1.2	0.70	1927	1.1	70	0.033	0.71	0.68
'HK-13'	2	0.040	0.90	0.50	1954	0.8	100	0.043	0.82	0.58
'HK-14'	2.5	0.040	1.0	0.60	2132	0.9	94	0.038	0.79	0.62
'SLY-1'	2	0.030	1.3	0.70	2338	0.9	96	0.034	0.66	0.76
'SLY-2'	2.5	0.030	1.2	0.70	1819	1.1	68	0.033	0.69	0.81
'SLY-3'	2	0.020	0.60	0.50	2169	0.9	116	0.041	0.95	0.64
'SLY-5'	5	0.040	0.90	0.60	2009	1.1	84	0.036	0.84	0.75
'SLY-6'	2	0.070	0.90	0.60	2422	0.8	136	0.045	0.85	0.85
'SLY-7'	3	0.050	0.90	0.70	2098	1.0	89	0.037	0.83	0.79
'QE-3'	2	0.020	1.0	0.90	1527	1.7	37	0.025	0.81	0.78
'QE-4'	2	0.020	0.90	1	1839	1.6	45	0.024	0.82	0.75
'QE-5'	2	0.17	0.90	0.90	1983	1.5	55	0.026	0.84	0.77
Liquid N_2O Firing Tests (Conducted Using Hokkaido University Facilities)										
'CBX-2'	2.5	0.050	1.7	1.6	2652	1.8	50	0.015	0.21	0.87
'CBX-3'	2.6	0.040	2.2	2.6	2067	3.4	21	0.0080	0.12	0.77
'CBX-4'	3.3	0.12	2.0	2.6	2190	3.3	23	0.0090	0.15	0.72
'CBX-5'	3	0.080	2.0	2.6	1755	4.1	15	0.0080	0.14	0.69
'CBX-6'	2.5	0.040	1.8	2.5	2011	3.5	21	0.010	0.18	0.84
'CBX-7'	3.5	0.040	1.8	2.4	1853	3.8	18	0.010	0.18	0.90
'CBX-8'	4	0.060	1.8	2.5	1869	3.8	18	0.0090	0.18	0.87
'CBX-9'	3	0.070	1.8	2.4	2192	3.1	25	0.010	0.19	0.83
'CBX-10'	2	0.14	1.2	2	2296	2.8	34	0.014	0.30	0.84
'CBX-11'	2.5	0.14	1.1	1.6	2280	2.3	43	0.018	0.31	0.81

'CBX-12'	2.3	0.18	1.3	2.6	1604	5.0	14	0.010	0.27	0.78
'CBX-13'	1.5	0.20	1.1	2.5	2015	4.3	21	0.011	0.32	0.80
'CBX-14'	2	0.17	1.0	2.0	3146	2.2	61	0.016	0.33	0.85
'CBX-16'	2	0.14	0.90	1.6	1851	3.0	33	0.017	0.34	0.85
LOX Firing Tests (Conducted Using Uematsu Electric Company Facilities)										
'ERM-2'	3	0.16	1.9	1.2	1982	1.4	42	0.024	0.36	1.04
'ERM-3'	2.5	0.10	1.2	1.2	2273	1.6	51	0.029	0.71	0.93
'ERM-4'	2.5	0.29	0.90	1.1	1820	2.0	40	0.029	0.86	0.95
'ERM-5'	2.5	0.22	0.30	0.8	1564	1.8	44	0.032	1.00	0.84
'ERM-6'	1.5	0.12	0.60	1.0	1154	2.8	21	0.028	0.96	0.90
'ERM-8'	1.5	0.35	1.2	1.6	2121	2.2	35	0.022	0.73	1.04
'ERM-10'	4	0.090	0.50	0.8	2142	1.2	75	0.039	0.99	1.04
'MSS-2'	0	0	1.8	1.9	1725	2.7	20	0.015	0.38	1.02
'MSS-3'	5	0.19	1.7	1.9	1994	2.4	26	0.018	0.46	1.07
'MSS-4'	6	0.26	1.4	1.7	2228	2.1	36	0.021	0.60	1.06
'MSS-5'	7	0.30	1.2	1.5	2550	1.7	53	0.026	0.68	1.08
'MSS-6'	7	0.24	1.4	1.9	2266	2.3	34	0.020	0.63	1.09
'MSS-8'	0	0.010	3.4	1.7	1587	2.0	20	0.0090	0.05	0.97
'MSS-9'	3	0.36	2.4	1.7	2275	1.5	37	0.015	0.17	1.07

REFERENCES

[1] D. R. Bartz, “A Simple Equation for Rapid Estimation of Rocket Nozzle Convective Heat Transfer Coefficients,” *J. Jet Propuls.*, vol. 27, no. 1, pp. 49–51, 1957.

[2] D. R. Bartz, “Turbulent Boundary-Layer Heat Transfer from Rapidly Accelerating Flow of Rocket Combustion Gases and of Heated Air,” *Adv. Heat Transf.*, vol. 2, no. C, pp. 1–108, 1965.

[3] G. P. Sutton and O. Bibliarz, *Rocket Propulsion Elements*, 8th ed. John Wiley & Sons, Inc., 2010.

[4] H. G. Price, “Cooling of High-Pressure Rocket Thrust Chambers With Liquid Oxygen,” *J. Spacecr. Rockets*, vol. 18, no. 4, pp. 338–343, 1980.

[5] H. G. Price and P. A. Masters, “Liquid Oxygen Cooling of High Pressure LOX / Hydrocarbon Rocket Thrust Chambers,” 1986.

[6] E. Armstrong and J. Schlumberger, “Cooling of Rocket Thrust Chambers With Liquid Oxygen,” 1990.

[7] J. D. Batchelor and E. L. Olcott, “Failure Mechanisms in Dense Tungsten Alloy Rocket Nozzles,” *J. Spacecr. Rockets*, vol. 1, no. 6, pp. 635–642, 1964.

[8] J. R. Johnston, R. A. Signorelli, and J. C. Freche, “Performance of Rocket Nozzle Materials With Several Solid Propellants,” Washington, D. C., 1966.

[9] W. D. Klopp, “Materials,” in *Exploring in Aerospace Rocketry*, National Aeronautics and Space Administration, Washington, D.C., 1971, pp. 79–94.

[10] H. O. Pierson, *Handbook of Carbon, Graphite, Diamond and Fullerenes: Properties, Processing and Applications*. Park Ridge, New Jersey: Noyes Publications, 1993.

[11] R. L. Bailey and E. G. Parks, JR., “Evaluation of Concepts for Reuse of Large Booster Nozzles.,” *J. Spacecr. Rockets*, vol. 5, no. 5, pp. 577–582, 1969.

[12] N. A. Kimmel, “Alternate Nozzle Ablative Materials Program,” 1984.

[13] L. B. Powers and R. L. Bailey, “Shuttle Subscale Ablative Nozzle Tests,” *J. Spacecr. Rockets*, vol. 19, no. 2, pp. 104–112, 1982.

[14] D. Altman, “Overview and History of Hybrid Rocket Propulsion,” in *Fundamentals of Hybrid Rocket Combustion and Propulsion*, M. J. Chiaverini and K. K. Kuo, Eds. AIAA, 2007, pp. 1–36.

[15] K. K. Kuo and M. Chiaverini, “Challenges of Hybrid Rocket Propulsion in the 21st Century,” in *Fundamentals of Hybrid Rocket Combustion and Propulsion*, M. J. Chiaverini and K. K. Kuo, Eds. AIAA, 2007, pp. 593–638.

[16] S. D. Eilers, S. Whitmore, and Z. Peterson, “Multiple Use Hybrid Rocket Motor,” US2014/0026537A1, 2014.

[17] N. Quigley and J. E. Lyne, “Development of a Three-Dimensional Printed, Liquid-Cooled Nozzle for a Hybrid Rocket Motor,” *J. Propuls. Power*, vol. 30, no. 6, pp. 1726–1727, 2014.

[18] P. Lemieux, “Nitrous Oxide Cooling in Hybrid Rocket Nozzles,” *Prog. Aerosp. Sci.*, vol. 46, no. 2–3, pp. 106–115, 2010.

[19] G. Ercole, E. Garofalo, P. Lemieux, M. M. Maglie, and D. Pastrone, “N2O-Cooled Aerospike for a Hybrid Rocket Motor: Nitrous Oxide Characterization and Additive Manufacturing,” no. July, pp. 1–18, 2017.

[20] A. Kumar, V. Saini, P. R. Usurumarti, and R. S. Dondapati, “Feasibility Studies on the Cooling of Hybrid Rocket Nozzles Using Supercritical Nitrous Oxide,” *Energy Procedia*, vol. 109, pp. 338–345, 2017.

[21] D. Bianchi and F. Nasuti, “Numerical Analysis of Nozzle Material Thermochemical Erosion in Hybrid Rocket Engines,” *J. Propuls. Power*, vol. 29, no. 3, pp. 547–558, 2013.

[22] S. Gordon and B. J. McBride, “Computer Program for Calculation of Complex Chemical Equilibrium Compositions,” 1994.

[23] L. Meyer, “The Surface Reaction of Graphite of Graphite With Oxygen Carbon Dioxide and Water Vapour at Low Pressures,” *Trans. Faraday Soc.*, vol. 34, no. 1056, pp. 1056–1061, 1938.

[24] R. F. Strickland-Constable, “The Oxidation of Carbon by Nitrous Oxide,” *Trans. Faraday Soc.*, vol. 34, no. 1374, pp. 1374–1384, 1938.

[25] R. F. Strickland-Constable, “The Interaction Oxygen and Carbon Filaments at High Temperatures,” *Trans. Faraday Soc.*, vol. 40, pp. 333–343, 1944.

[26] J. S. Binford and H. Erying, “Kinetics of the Steam-Carbon Reaction,” *J. Phys. Chem.*, vol. 63, no. 5, pp. 693–696, 1959.

[27] L. J. Delaney, L. C. Eagleton, and W. H. Jones, “A Semiquantitative Prediction of the Erosion of Graphite Nozzle Inserts,” *AIAA J.*, vol. 2, no. 8, pp. 1428–1433, 1964.

[28] A. J. McDonald and P. O. Hedman, “Erosion of Graphite in Solid-Propellant Combustion Gases and Effects on Heat-Transfer,” *AIAA J.*, vol. 3, no. 7, pp. 1250–1257, 1965.

[29] J. L. Mayberry, J. W. Kordig, R. J. Zeamer, and S. C. Bro, “Correlation of Graphite Nozzle Throat Erosion in Solid-Rocket Motors.,” *AIAA J.*, vol. 6, no. 11, pp. 2222–2224, 1968.

[30] S. R. Turns, *An Introduction to Combustion: Concepts and Applications*, 3rd ed. New York, NY: McGraw-Hill, 2012.

[31] S. T. Keswani, E. Andiroglu, J. D. Campbell, and K. K. Kuo, “Recession Behavior of Graphitic Nozzles in Simulated Rocket Motors,” *J. Spacecr. Rockets*, vol. 22, no. 4, pp. 396–397, 1985.

[32] L. E. Jones, P. A. Thrower, and P. L. Walker, “Bulk Graphite Nozzle Recession-An analysis Based on the Carbon-Steam Reaction,” *Carbon N. Y.*, vol. 24, no. 1, pp. 43–49, 1986.

[33] V. Borie, J. Brulard, and G. Lengelle, “Aerothermochemical Analysis of Carbon-Carbon Nozzle Regression in Solid-Propellant Rocket Motors,” *J. Propuls. Power*, vol. 5, no. 6, pp. 665–673, 1989.

[34] R. Acharya and K. K. Kuo, “Effect of Chamber Pressure and Propellant Composition on Erosion Rate of Graphite Rocket Nozzle,” *J. Propuls. Power*, vol. 23, no. 6, pp. 1242–1254, 2007.

[35] P. Thakre and V. Yang, “Chemical Erosion of Carbon-Carbon/Graphite Nozzles in Solid-Propellant Rocket Motors,” *J. Propuls. Power*, vol. 24, no. 4, pp. 822–833, 2008.

[36] D. Bianchi, F. Nasuti, M. Onofri, and E. Martelli, “Thermochemical Erosion Analysis for Chraphite/Carbon-Carbon Rocket Nozzles,” *J. Propuls. Power*, vol. 27, no. 1, pp. 197–205, 2011.

[37] L. Kamps *et al.*, “Method for Determining Nozzle-Throat-Erosion History in Hybrid Rockets,” *J. Propuls. Power*, vol. 33, no. 6, pp. 1369–1377, 2017.

[38] B. Evans, “Nozzle Erosion Characterization and Minimization For High-Pressure Rocket Motor Applications,” Pennsylvania State University, 2010.

[39] D. Bradley, G. Dixon-Lewis, S. El-din Habik, and E. M. J. Mushi, “The Oxidation of Graphite Powder in Flame Reaction Zones,” *Symp. Combust.*, vol. 20, no. 1, pp. 931–940, 1985.

[40] H. K. Chelliah, A. Makino, I. Kato, N. Araki, and C. K. Law, “Modeling of Graphite Oxidation in a Stagnation-Point Flow Field Using Detailed Homogeneous and Semiglobal Heterogeneous Mechanisms with Comparisons to Experiments,” *Combust. Flame*, vol. 104, no. 4, pp. 469–480, 1996.

[41] B. R. Bird, W. E. Stewart, and E. N. Lightfood, *Transport Phenomena*, 2nd ed. New York, NY: John Wiley & Sons, Inc., 2001.

[42] E. R. Gilliland and T. K. Sherwood, “Diffusion of Vapors into Air Streams,” *Ind. Eng. Chem.*, vol. 26, no. 5, pp. 516–523, 1934.

[43] K. Ozawa and T. Shimada, “Effects of O/F Shifts on Flight Performances of Vertically Launched Hybrid Sounding Rockets,” in *53rd AIAA/SAE/ASEE Joint Propulsion Conference*, 2017.

[44] L. T. Kamps *et al.*, “Investigation of Graphite Nozzle Erosion in Hybrid Rockets Using O2/C2H4,” *2018 Jt. Propuls. Conf.*, pp. 1–24, 2018.

[45] F. Cauty and D. Gramer, “Solid-Fuel Pyrolysis Phenomena and Regression Rate, Part 2: Measurement Techniques,” in *Fundamentals of Hybrid Rocket Combustion and Propulsion*, 2012, pp. 167–206.

[46] E. J. Wernimont and S. D. Heister, “Reconstruction Technique for Reducing Hybrid-Rocket Combustion Test Data,” *J. Propuls. Power*, vol. 15, no. 1, pp. 128–136, 1999.

[47] H. Nagata, H. Nakayama, M. Watanabe, M. Wakita, and T. Totani, “Accuracy and Applicable Range of a Reconstruction Technique for Hybrid Rockets,” *Adv. Aircr. Spacecr. Sci.*, vol. 1, no. 3, pp. 273–289, 2014.

[48] C. Carmicino and A. R. Sorge, “Influence of a Conical Axial Injector on Hybrid Rocket Performance,” *J. Propuls. Power*, vol. 22, no. 5, pp. 984–995, 2006.

[49] H. Nagata, Y. Saito, T. Ishiyama, Y. Inaba, M. Wakita, and T. Totani, “Evaluations of Data Reduction Methods for Hybrid Rockets Harunori,” *65th Int. Astronaut. Congr.*, 2014.

[50] L. Kamps and H. Nagata, “Estimation of Nozzle Throat Wall Temperature History in Hybrid Rockets,” no. 1.

[51] Y. Saito, T. Uematsu, H. Isochi, M. Wakita, T. Totani, and H. Nagata, “Estimation of Hybrid Rocket Nozzle Throat Erosion History,” *Trans. Japan Soc. Aeronaut. Sp. Sci. Aerosp. Technol. Japan*, vol. 14, no. ists30, p. Pa_145-Pa_151, 2017.

[52] L. Kamps, K. Sakurai, Y. Saito, and H. Nagata, “Comprehensive Data Reduction for N2O/HDPE Hybrid Rocket Motor Performance Evaluation,” *Aerospace*, vol. 6, no. 4, p. 45, 2019.

[53] R. C. Mehta, “Estimation of Heat-Transfer Coefficient in a Rocket Nozzle,” *AIAA J.*, vol. 19, no. 8, pp. 1085–1086, 1981.

[54] P. Narsai, E. Momanyi, K. Venkataraman, B. J. Evans, and B. J. Cantwell, “Indirect Heat Flux Measurements at the Nozzle Throat of a Hybrid Rocket Motor,” in *51st AIAA/SAE/ASEE Joint Propulsion Conference*, 2015.

[55] “ISOTROPIC GRAPHITE: Typical Properties.” [Online]. Available: https://www.tokaicarbon.co.jp/en/products/fine_carbon/pdf/Isotropic_graphite.pdf. [Accessed: 13-Jun-2018].

[56] A. I. Lutcov, V. I. Volga, and B. K. Dymov, “Thermal conductivity, electric resistivity and specific heat of dense graphites,” *Carbon N. Y.*, vol. 8, no. 6, pp. 753–760, 1970.

[57] A. T. D. Butland and R. J. Maddison, “The Specific Heat of Graphite: An Evaluation of Measurements,” *J. Nucl. Mater.*, vol. 49, pp. 45–56, 1973.

[58] W. S. Rasband, “ImageJ.” U.S. National Institutes of Health, Bethesda, MD, USA, 1997.

[59] R. Pasztor, “Richard Branson’s Space-Tourism Company Rockets Out of Atmosphere for First Time,” *The Wall Street Journal*, 2018.

[60] A. Takahashi and T. Shimada, “Essentially Non-Explosive Propulsion Paving a Way for Fail-Safe Space Transportation,” *Trans. Japan Soc. Aeronaut. Sp. Sci. Aerosp. Technol. Japan*, vol. 16, pp. 1–8, 2018.

[61] E. T. Jens, B. J. Cantwell, and G. S. Hubbard, “Hybrid Rocket Propulsion Systems for Outer Planet Exploration Missions,” *Acta Astronaut.*, vol. 128, pp. 119–130, 2016.

[62] E. T. Jens, A. C. Karp, S. Contadin, A. Conte, B. Nakazono, and D. Vaughan, “Development Testing of Hybrid Rocket Motors Using Classical Fuels for Interplanetary CubeSats,” no. July, pp. 1–16, 2017.

[63] E. T. Jens, A. C. Karp, J. Rabinovitch, A. Conte, B. Nakazono, and D. A. Vaughan, “Design of Interplanetary Hybrid CubeSat and SmallSat Propulsion Systems,” pp. 1–18, 2018.

[64] S. Heister and E. Wernimont, “Hydrogen Peroxide, Hydroxyl Ammonium Nitrate and Other Storable Oxidizers,” in *Fundamentals of Hybrid Rocket Combustion and Propulsion*, American Institute of Aeronautics and Astronautics, Inc., 2007, pp. 457–487.

[65] G. Story and J. Arves, “Flight Testing of Hybrid-Powered Vehicles,” in *Fundamentals of Hybrid Rocket Combustion and Propulsion*, 2007, pp. 553–592.

[66] M. Kobald *et al.*, “Sounding Rocket ‘HEROS’ - A Low-Cost Hybrid Rocket Technology Demonstrator,” no. July, pp. 1–26, 2017.

[67] Y.-S. Chen and B. Wu, “Development of a Small Launch Vehicle with Hybrid Rocket Propulsion,” no. July, pp. 9–11, 2018.

[68] G. Zilliac, B. S. Waxman, A. M. Karabeyoglu, B. Cantwell, and B. J. Evans, “Peregrine Hybrid Rocket Motor Development,” pp. 1–17, 2014.

[69] H. Gamal, A. Matusiewicz, R. Magiera, D. Hubert, and L. Karolewski, “Design, Analysis and Testing of a Hybrid Rocket Engine with a Multi-Port Nozzle,” pp. 1–15, 2018.

[70] H. Nagata, M. Wakita, T. Totani, and T. Uematsu, “Development and Flight Demonstration of 5 kN Thrust Class CAMUI Type Hybrid Rocket,” *Trans. Japan Soc. Aeronaut. Sp. Sci. Aerosp. Technol. Japan*, vol. 12, no. ists29, p. Ta_1-Ta_4, 2014.

[71] L. Kamps and H. Nagata, “Tubular Equivalent Regression Rate in Hybrid Rockets with Complex Geometries,” *Trans. Japan Soc. Aeronaut. Sp. Sci. Aerosp. Technol. Japan*, 2019.

[72] A. Mazzetti, L. Merotto, and G. Pinarello, “Paraffin-based hybrid rocket engines applications: A review and a market perspective,” *Acta Astronaut.*, vol. 126, pp. 286–297, 2016.